Rijksuniversiteit Groningen

Master Thesis

Secondary to primary flux ratios as a tool to understand cosmic-ray transport

Author:
J. Jongejan

Supervisor:
Dr. M. Vecchi

ACKNOWLEDGEMENTS

ON A PROFESSIONAL NOTE I WOULD LIKE TO AKNOWLEDGE

Dr. Manuela Vecchi for her guiding and endless patience in the process of conducting research and writing. I greatly value her support and optimism that helped me through the project.

Eduardo Ferronato Bueno for his technical assistance regarding the scripts used in this project.

The Center For Information Technology of the University of Groningen for their support and for providing access to the Peregrine high performance computing cluster.

Abstract

The unprecedented percent precision measurements of the current generation space-based experiments revealed unexpected features in galactic cosmic-ray (CR) fluxes. These new data have been used to constraint CR propagation in the galaxy. New benchmark scenarios have been derived in Genolini et al. 2019 for galactic CR propagation in view of the Boron to Carbon flux ratio from the Alpha Magnetic Spectrometer (AMS-02), based on fits to data using the USINE software. This semi-analytic code is freely available online, and it allows to compare the importance of various ingredients on cosmic-ray fluxes and flux ratios. Moreover, it enables to select cosmic-ray transport models and the user's configurations to fit data with any number of free parameter and nuisance parameters. In this work, we have achieved two main results. First, we have followed the method presented in Derome et al. 2019 to study the effect of cross-sections on the determination of propagation parameters. We generate and analyse mock data comparable to the B/C measurements performed by the AMS-02 experiment, using three benchmark models, BIG, SLIM, and QUAINT available in the literature. We show that detailed information of the nuclear cross-sections is essential to avoid biases in the analysis. Moreover, we have further constrained the propagation parameters using two additional observables, namely the deuteron flux and the ^{2}H/^{4}He flux ratio, which are helpful to test the universality of CR propagation in the galaxy. We studied how the deuteron flux depends on the galactic disk size, the solar modulation effective potential, the choice of the transport model, and various physical processes relevant to CR propagation through the galaxy. We fit the deuteron flux and the ^{2}H/^{4}He flux ratio models to the current best measurements from the PAMELA experiment. We obtained constraints on the propagation parameters for the three benchmark models. Our results are overall consistent with those obtained in the literature from the B/C flux ratio, even though we observe some tension. The inclusion of cross-section nuisance parameters together with upcoming AMS-02 measurements are necessary to assess stricter constraints on the transport parameters.

This manuscript is structured as follows. Section 1 provides an introduction to cosmic-ray origin and propagation, together with an overview of the recent data and the relevant literature. Section 2 describes the three cosmic-ray transport benchmark models BIG, SLIM and QUAINT and the USINE software that is used in this project. Section 3 presents our results the effect of cross-sections on the determination of propagation parameters. Section 4 shows our results on the analysis of observables ^{2}H and ^{2}H/^{4}He. Finally the conclusions in Section 5.

Contents

1 Introduction

High-energy charged particles that originate from outer space are observed on Earth. We call these particles cosmic rays (CRs). The number of particles observed per unit energy, per unit area, per unit time and per unit solid angle is called the flux or spectrum and can be displayed as a function of the energy of the observed particles. This spectrum can be described as a power-law in energy, i.e. $\Phi \propto E^{-\gamma}$ where γ is the spectral index. However, the spectrum shows several features that indicate that a single power-law is not enough to describe it. To emphasise the deviations from the single power-law often the CR flux is rescaled by the pure power-law. Figure 1 shows such a spectrum at the GeV-TeV range, measured by AMS and other experiments [1]. CRs at these energies have a galactic origin because their energies are not enough to escape the galactic confinement and are mainly made of CR protons (90%). The second largest component is He which accounts for about 8% of the total and a few percent are heavier species, up to Fe. A small component of about 1% is accouted for by electrons and antimatter. The CRs with GeV-TeV energies are detected with space-born detectors where the flux of these particles is of the order of one particle per square meter per second and therefore high enough to observe a reasonable amount of particles over a time span of several years. However, the flux decreases rapidly above TeV energies because these CRs have an extragalactic origin and in order to observe sufficiently many CR particles, we need detectors that are too large to launch into space. Therefore higher energy CRs in the range of $10^{15} - 10^{20}$ eV are detected indirectly with ground-based detectors observing air showers induced by the CRs.

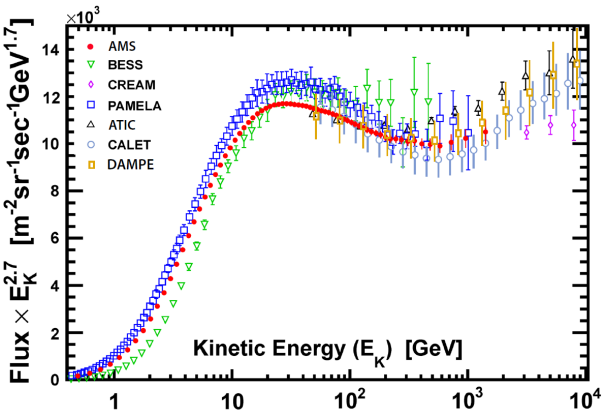

Figure 1: The latest AMS proton flux measurement together with the measurements from the recent other experiments in the entire energy range up to 1800 GeV. [1]

Figure 2 shows the CR flux above PeV energies from air shower measurements. It is referred to as the all-particle spectrum as it shows the particle flux a function of E (energy-per-nucleus) over seven orders of magnitude in energy in the range $10^{13} - 10^{20}$ eV. The vertical axis is rescaled by $E^{2.6}$ in order to emphasise deviations from a single power-law. The spectral feature that shows steepening of the spectrum between 10^{15} and 10^{16} eV is known as the *knee* of the spectrum. This could be explained by the maximum energy range up until which supernova remnants (SNRs) can accelerate particles ($\sim$ 15 TeV) [2]. Confinement of CRs in the Galaxy would be a possible explanation to the *second knee* ($\sim 10^{17}$ eV) due to measurement of an increase of heavy primaries at this energy [3]. The *ankle*, located between 10^{18} and 10^{19} eV, is considered to mark the end of the galactic component of CRs and the GZK effect is generally believed to be responsible for the highest energy cutoff [4, 5]. Protons with energies $E > 6 \cdot 10^{19}$ eV will scatter off CMB photons,

producing pions in the collision, i.e. $p + \gamma_{CMB} \rightarrow p + \pi^0$ or $p + \gamma_{CMB} \rightarrow n + \pi^+$.

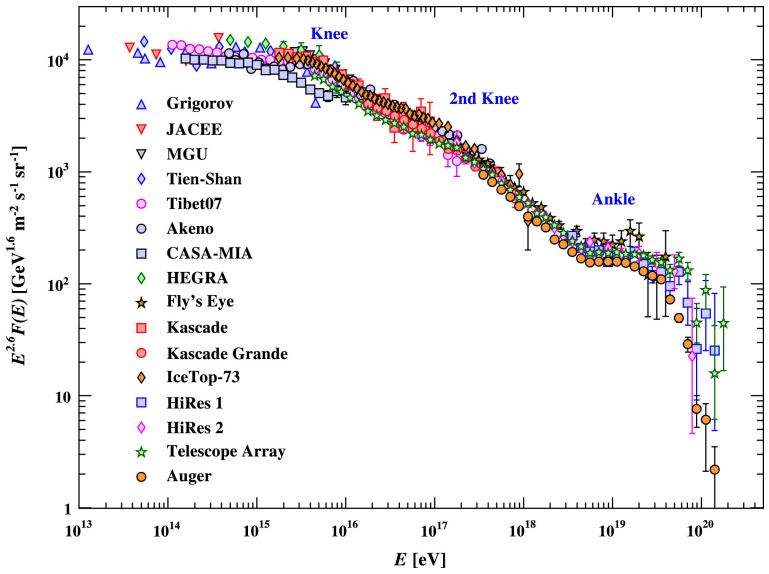

Figure 2: The all-particle spectrum as a function of E (energy-per-nucleus) from air shower measurements. [6]

Besides the observed CR flux, the composition of CR species can also provide insight to the production and propagation mechanisms. Cosmic rays can be divided into two broad classes: primary species, such as carbon and oxygen, are those accelerated at the sources, while secondary species, such as boron and lithium, are those produced as a consequence of nuclear interactions of primary species while propagating through the interstellar medium (ISM). The most promising observable to study the propagation of CRs in the Galaxy is studying secondary species or the flux ratio of a secondary species to a primary one. Figure 3 shows the composition of galactic CRs compared to the solar abundance of elements. One can observe the discrepancy mainly for elements Li, Be and B, and also the sub-Fe elements show a discrepancy, although less pronounced.

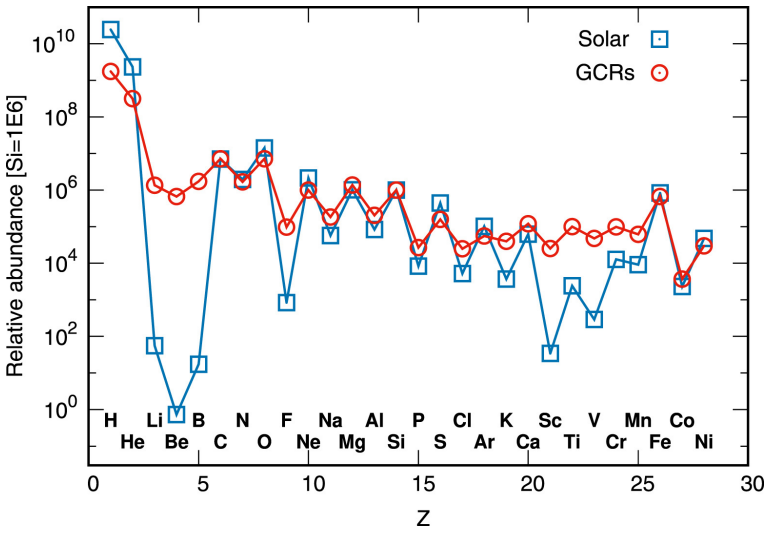

Figure 3: Relative abundances of the elements from H to Ni in the solar system and in low energy Galactic CRs [7].

These elements are secondary species as they originate from CR interactions with the interstellar medium. Therefore these elements are of interest in CR propagation studies. The measurement of the Boron-to-Carbon flux ratio, B/C in the following, has been widely used to test propagation scenarios. The first evidence for a break in the B/C was found by [8, 9]. This break most probably originates from a transition of diffusion regime rather than from source effects [10].

Investigation of the energy dependence of the spectrum and the composition of CR species can help us understand the ongoing physical processes responsible for the production and propagation of CRs. In the following we describe what are believed to be the most important sources and propagation mechanisms, as well as the experimental data relevant to this project.

1.1 The sources of cosmic rays

The Sun is a source of CRs with energies up to the 100 GeV [11] as a result of the modulation imposed by the presence of a magnetised wind originated from the Sun, which affects the propagation of very low energy particles and prevents them from reaching the solar system (12). These energies are relevant for the analysis of the data used in this project. One of the mechanisms producing CRs in sunspots is the cyclotron mechanism.
Turbulent plasma motions in the Sun generate magnetic fields [12]. Maxwell's equations tell us that change in the magnetic field generates and electric field and vice versa. During the creation and decay of the magnetic fields in sunspots an electric field is generated that can accelerate charged particles, mainly the protons and electrons of which the plasma exists. To quantify this effect, we look at Figure 4a. A sunspot with area $A = \pi R^2$ and a time-varying magnetic field $\vec{B}$ is considered together with a charged particle that travels around the time-varying magnetic field. The magnetic flux ϕ is given by

$$\phi = \int \vec{B} \cdot d\vec{A} = B\pi R^2 \tag{1}$$

where $d\vec{A}$ is an infinitesimal surface element of the sunspot. The magnetic flux changes over time and creates a potential U

$$U = -\frac{d\phi}{dt} = \oint \vec{E} \cdot d\vec{s} \tag{2}$$

where $\vec{E}$ is the electric field and $d\vec{s}$ is an infinitesimal distance along the particle trajectory. Assume that the magnetic field is perpendicular to the surface area of the sunspot, i.e. $\vec{B} \parallel \vec{A}$ hence $\vec{B} \cdot \vec{A} = BA$, and combine equations 1 and 2. We obtain the energy gained by the particle after one turn around the magnetic field

$$E = eU = e\pi R^2 \frac{d\phi}{dt} \tag{3}$$

For typical sunspots ($R = 10^7$ m, $\frac{dB}{dt} = 2000$ G/day) this leads to an energy gain $E = 0.73$ GeV. This mechanism produces CRs with energies at the lower end of the energy range of the data used for the analysis in this project.

Other sources of solar CRs are sunspot pairs. Pairs of sunspots of opposite magnetic polarity often occur, depending on the phase of the 11 year solar cycle. Consider two sunspots approaching each other before merging and assume one of them is at rest. Then the second creates an electric field perpendicular to the direction of the magnetic dipole and perpendicular

to the direction of its motion $\vec{v}$. Consequently, the electric field generated is parallel to $\vec{v} \times \vec{B}$. The situation is visualised in Figure 4b. Typical solar conditions lead to electric fields of 10 V/m. Due to low density conditions in the chromosphere (the thin solar atmospheric layer above the thick photosphere from which photons escape the Sun) particles experience less collisional energy losses than the energy gained from the electric field that accelerates them.

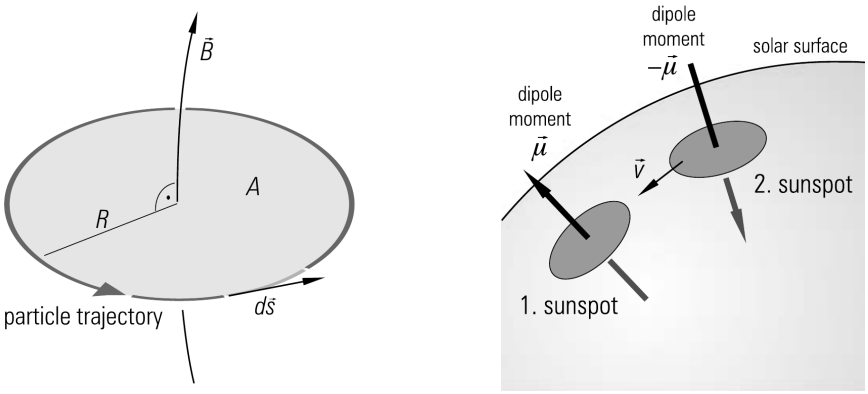

(a) (b)

Figure 4: (a) Principle of particle acceleration by variable sunspots. (b) Sketch of a sunspot pair. [11]

We can also consider galactic sources of CRs. Supernova remnants (SNRs) generate shock waves that can accelerate charged particles up to high energies through the first order Fermi mechanism and they are believed to be the most important sources of CRs. The main reason for this is that the energy released in the explosion is $E_{SN} \approx 10^{51}$ erg and if only 10% of the energy is transferred via a diffusive shock to the ambient medium, this can explain the CR source spectrum up to TeV energies. [13] Diffusive shock acceleration in SNRs can be described by the first order Fermi mechanism that is explained later.

Long after the shock wave has dissipated its energy into the ISM, the remaining core of the collapsed star is still able to generate CRs. When a star goes supernova, it implodes and shrinks to a size in the order of kilometers. What is left is a pulsar, a magnetised neutron star with an extraordinarily small rotational period in the order of miliseconds due to conservation of angular momentum during its collapse. In general the axis of rotation is not aligned with the direction of the magnetic field. Due to the fast rotation and extraordinarily strong magnetic field, strong electric fields of magnitude

$$|\vec{E}| = vB\sin(\theta) = \frac{2\pi R_{pulsar}}{T_{pulsar}} B\sin(\theta) \tag{4}$$

are produced, where θ represents the angle between the rotational axis and the direction of the magnetic field. For a pulsar with $T_{pulsar} = 30$ ms, $R = 20$ km, $B = 2.5 \cdot 10^8$ T, electric fields of $|\vec{E}| = 10^{15}\ \mathrm{V\,m^{-1}} \sin(\theta)$ can be created. This leads to a hypothetical energy gain of $E = 1$ $\mathrm{PeV\,m^{-1}}$. Therefore pulsars are a plausible potential source of observed CRs.

Finally we consider binary stars that are a combination of a pulsar or neutron star together with a normal star are considered an extragalactic source of CRs. In such a system large amounts of stellar matter from the normal star transferred to the pulsar or neutron star onto an accretion

disk. The accretion disk consists of an ionised plasma orbiting the compact object, generating strong electromagnetic fields. The variable magnetic field of the pulsar together with the large scale plasma motions create strong electric fields. With reasonable assumptions, these binary systems can accelerate particles to $E = 3 \cdot 10^{18}$ eV [14]. An even more extreme situation based on the same process can be found in active galactic nuclei (AGNs). An accretion disk surrounding the central black hole of a galaxy in this case causes strong electromagnetic fields. These objects are believed to be the origin of the most energetic primaries in the universe that have been observed [15].

1.2 Confinement and acceleration in the Galaxy

Different astrophysical processes can accelerate particles to a wide range of energies. However, the detection of these particles and the flux we observe, depends on how long the particles stay confined in the galactic magnetic field. Whether a particle is confined in a magnetic field can be determined by comparing its Larmor radius with the size of the region in which the particle might be confined. The Larmor radius is the radius of the circular motion of a charged particle in the presence of a uniform magnetic field and it is obtained by equating the Lorentz force on the charged particle to its centripetal force. For a uniform static magnetic field, we can write the magnitude of the Lorentz force F_L as

$$\vec{F_L} = \frac{d}{dt}\gamma m_0 \vec{v} = \gamma m_0 \frac{d\vec{v}}{dt} = Ze(\vec{v} \times \vec{B}) = Ze|\vec{v}||\vec{B}|\sin(\theta)(\hat{i}_v \times \hat{i}_B) \tag{5}$$

where ze is the particle charge and θ the pitch angle of the particle's orbit. Unit vectors $\hat{i}_v$ and $\hat{i}_B$ indicate the direction of the velocity and magnetic field, respectively. Equating the acceleration due to the Lorentz force to the centripetal acceleration gives

$$\frac{v_\perp^2}{r} = \frac{Ze|\vec{v}||\vec{B}|\sin(\theta)}{\gamma m_0} \tag{6}$$

Rearranging and substituting the relativistic three-momentum of the particle $p = \gamma m_0 |\vec{v}|$ leads to an expression for the Larmor radius, also called gyroradius or cyclotron radius

$$r_L = \frac{\gamma m_0 |\vec{v}|\sin(\theta)}{Ze|\vec{B}|} = \left(\frac{pc}{Ze}\right)\frac{\sin(\theta)}{|\vec{B}|c} \tag{7}$$

where $\frac{pc}{Ze}$ is the particle rigidity $R = pc/Ze$. Formal derivation of the Larmor radius can be found in [16]. One can observe that the Larmor radius depends on the charge of the particle. The Larmor radius depends on the particle charge and is therefore different for nuclei of different species. A particle will stay confined in the acceleration region until its Larmor radius is smaller than the size of the actual accelerator. The Larmor radius inverse dependence on the particle charge (Ze) implies that lighter species are confined in a magnetic region (of size r_L) up until *higher energies* than heavy species, but up until the *same rigidity*. The energy dependence is displayed in Figure 5 and could be an explanation of the the knee in the all-particle spectrum. All CRs are sensitive to the same galactic magnetic field and therefore the containment radius depends on the atomic number. The position of the knee should depend on the charge of primary cosmic rays and we would expect the iron knee at higher energies than the proton knee. Adding up the fluxes for all CR species each with their knee feature at a certain energy leads to a spectrum with a broader knee region, as we observe in Figure 2.

Particles can gain energy as long as they are confined in acceleration regions, such as SNRs

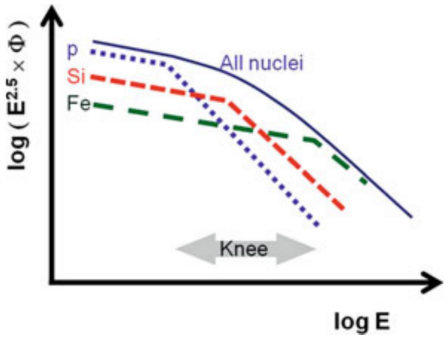

Figure 5: Interpretation of the knee as due to the dependence of the maximum energy on the nuclear charge Z. [17]

or magnetic clouds, via the first and second order Fermi mechanisms. The first order Fermi mechanism describes the acceleration of charged particles by shock waves, of which SNRs are astrophysical sources. Consider a shock wave originating from a SNR interacting with the ISM and the shock front travels with velocity u_1 with respect to the ISM. Behind the shock front the gas heated by the shock wave recedes at velocity u_2. In the laboratory frame the speed of the gas is then $u_1 - u_2$. This is visualised schematically in Figure 6a.

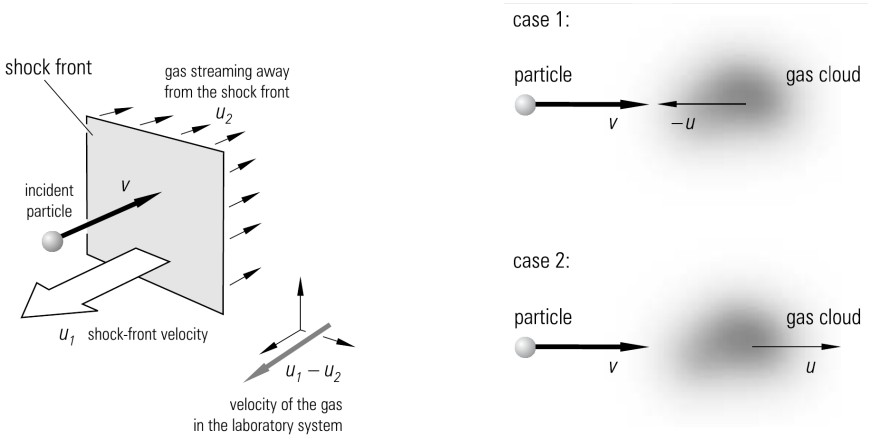

(a) (b)

Figure 6: (a) First order Fermi mechanism: schematics of shock-wave acceleration. (b) Second order Fermi mechanism: energy gain of a particle by a reflection from a magnetic cloud. [11]

If a particle collides with the shock front at velocity v and gets reflected, the energy is given by

$$\Delta E = \frac{1}{2}m(v + (u_1 - u_2))^2 - \frac{1}{2}mv^2 = \frac{1}{2}m(2v(u_1 - u_2) + (u_1 - u_2)^2) \tag{8}$$

which results in a relative energy gain of

$$\frac{\Delta E}{E} \approx \frac{2(u_1 - u_2)}{v} \tag{9}$$

However, this is in the case of a non-relativistic approach. In reality the particles travel at relativistic speeds and encounter the shock wave at various angles. In this case the average relative energy gain can be expressed as [16]

$$\frac{\Delta E}{E} = \frac{4}{3}\frac{(u_1 - u_2)}{c} \tag{10}$$

One can also consider particles that are trapped between two shock fronts. Assume that the outer shock front moves at velocity v_1 smaller than the inner shock front that travels with velocity v_2, since the outer shock front has already been slowed down by interaction with the ISM. A particle reflected off the inner shock front gains energy E_1 and a particle reflected off the outer shock front loses energy E_2 as expressed in equations 11 and 12 respectively. This leads to an average energy gain of ΔE as expressed in equation 13.

$$\Delta E_1 = \frac{1}{2}m(v + v_2)^2 - \frac{1}{2}mv^2 = \frac{1}{2}m(v_2^2 + 2vv_2) \tag{11}$$

$$\Delta E_2 = \frac{1}{2}m(v - v_1)^2 - \frac{1}{2}mv^2 = \frac{1}{2}m(v_1^2 - 2vv_1) \tag{12}$$

$$\Delta E = \frac{1}{2}m(v_1^1 + v_2^2 + 2v(v_2 - v_1)) \tag{13}$$

Again the linear term dominates and quadratic terms can be neglected. Since $v_2 > v_1$, the energy gain reduces to $\Delta E \approx mv\Delta v$ and we obtain a relative energy gain

$$\frac{\Delta E}{E} \approx 2\frac{\Delta v}{v} \tag{14}$$

In both cases we find an energy gain depending on v, i.e. $\Delta E \sim \beta$. We find that the energy a particle gains from the encounter with a shock front depends on the velocity of the shock front. Consequently, the energy spectrum of CRs that we obtain from measurements is affected by this propagation mechanism.

The second order Fermi mechanism describes the acceleration of charged particles by collisions with moving magnetic clouds. Consider a particle with velocity $\vec{v}$ that gets reflected off a magnetic gas cloud with velocity $\vec{u}$ as visualised in Figure 6b. If the particle and gas cloud move in opposite direction, the energy gain of the particle ΔE_1 can be expressed as in equation 15. If the particle and gas cloud move in the same direction, the energy loss of the particle ΔE_2 can be expressed as in equation 16. The average energy gain ΔE and relative energy gain $\frac{\Delta E}{E}$ can then be expressed as in equations 17 and 18, respectively.

$$\Delta E_1 = \frac{1}{2}m(v + u)^2 - \frac{1}{2}mv^2 = \frac{1}{2}m(2uv + u^2) \tag{15}$$

$$\Delta E_2 = \frac{1}{2}m(v - u)^2 - \frac{1}{2}mv^2 = \frac{1}{2}m(-2uv + u^2) \tag{16}$$

$$\Delta E = \Delta E_1 + \Delta E_2 = mu^2 \tag{17}$$

$$\frac{\Delta E}{E} = 2\frac{u^2}{v^2} \tag{18}$$

We find an energy gain depending on u^2, i.e. $\Delta E \sim \beta^2$. Again we find that the energy a particle gains from the encounter with a shock front depends on the velocity of the shock front. Consequently, the energy spectrum of CRs that we obtain from measurements is also affected by this propagation mechanism.

The two acceleration mechanisms described above have several common points. In particular, the role of the magnetic fields is to confine the particles in the acceleration region. The particles are confined in the accelerator region for thousands of years before they can escape. The energy gain originates from the relative speed between the particle and the shock or cloud. For both mechanisms the energy losses are neglected and the particles escape from the acceleration regions if the Larmor radius of the particle is larger than the size of the region responsible for the acceleration.
The mechanisms differ from each other concerning the astrophysical environment in which the particles are accelerated. Also the speeds of the acceleration regions differ by orders of magnitude. Most importantly, the first order mechanism energy gain depends on β while the energy gain depends on β^2 for the second order mechanism. Even when the same velocity is assumed for the acceleration sites, the first order Fermi mechanism needs 10000 times less acceleration cycles (described below) than the second order mechanism to gain the same amount of energy [18]. Therefore we expect the first order mechanism to be much more important in the acceleration of primary CRs.
Theoretically a power spectrum of primary CRs is predicted. For a particle with initial energy E_0 that gains ϵE_0 per acceleration cycle the total energy gain after n cycles is

$$E_n = E_0(1+\epsilon)^n \qquad \Longleftrightarrow \qquad n = \frac{\ln\left(E/E_0\right)}{\ln(1+\epsilon)} \tag{19}$$

where n is the number of cycles required to accelerate a particle to final energy E_n. If we define the escape probability P, then the probability that a particle remains in the acceleration region is $(1-P)$. After n cycles, this probability is reduced to $(1-P)^n$. The number of particles in excess of final energy $E_n = E$ is then given by

$$N(>E) \sim \sum_{m=n}^{\infty}(1-P)^m = (1-P)^n \sum_{m=n}^{\infty}(1-P)^{m-n} = (1-P)^n \sum_{m=0}^{\infty}(1-P)^m = \frac{(1-P)^n}{P} \tag{20}$$

where in the last equality we made use of geometric series converging: $\sum_{r}^{\infty} x^r = \frac{1}{1-r}$ for $r < 1$. This gives the expected power spectrum of primary CRs

$$N(>E) \sim \frac{1}{P}\left(\frac{E}{E_0}\right)^{-\alpha} \sim E^{-\alpha} \tag{21}$$

where α is the spectral index that can be written as

$$\alpha = -\frac{n\ln(1-P)}{\ln(E/E_0)} = \frac{\ln(1/(1-P))}{\ln(1-P} \tag{22}$$

Acceleration by SNRs is considered the main mechanism for the production of primary CRs. The source injection can be parametrised by

$$q_a = Q_a E^{-\alpha} \tag{23}$$

where Q_a and α are the model parameters.

1.3 Propagation through the Galaxy

CRs undergo various physical processes between the moment they are accelerated in their sources (often SNRs) and the moment they hit our detectors. While propagating through the galaxy, CRs are prone to both spatial and momentum diffusion, convection processes, collisions with the ISM, radioactive decay and a veriety of processes which cause energy losses to the CRs. These potentially most important processes will be outlined below, starting with the spatial diffusion of CRs.

Charged particles interact with magnetic fields. Small variations $\delta B/B \ll 1$ in the magnetic fields cause CRs to scatter and diffuse isotropically and homogeneously. The particles diffused by a magnetic cloud will subsequently encounter another field and diffuse again. Repetition of this process makes the particles perform a random walk through the Galaxy. This can be described by combining a continuity equation with Fick's first law of diffusion [19], resulting in:

$$\left.\begin{aligned} \frac{\partial n}{\partial t} + \vec{\nabla}\cdot\vec{j} = 0 \qquad & \text{(continuity equation)} \\ \vec{j} = -K\vec{\nabla}n \qquad & \text{(Fick's law)} \end{aligned}\right\} \quad \Longrightarrow \quad \frac{\partial n}{\partial t} = \vec{\nabla}\cdot(K\vec{\nabla}n) \tag{24}$$

This is called the diffusion equation, in which n represents the CR density, $\vec{j}$ the diffusion current and K the diffusion coefficient. From quasi linear theory (QLT) we learn that the diffusion coefficient K can be described as

$$K = \frac{v\lambda}{3} = \frac{v}{3}\frac{r_L}{[\delta B/B]^2_{k_L}} \tag{25}$$

where v is the velocity of the particle, r_L the Larmor radius and $k_L \propto L^{-1}$ is the turbulence mode in resonance with the Larmor radius of the particle. The diffusion coefficient is inversely proportional to the square of the magnetic turbulence, i.e. $K \propto [\delta B/B]^{-2}_{k_L}$ [2, 20, 21]. Various types of magnetic turbulence can occur, resulting in different power spectra. In other words, the magnetic turbulence can be described by a power-law in energy $\Phi \propto E^{-\nu}$ where ν is the magnetic turbulence spectral index [22] that indicates the type of turbulence that is at play.
Kolmogorov theory predicts a power spectrum with spectral index $\nu = 5/3$ and relies on the assumption of incompressibility, which means that the velocity field of a fluid is solenoidal ($\vec{\nabla}\cdot\vec{u} = 0$). Turbulent motions can generally be composed in two main modes: longitudinal and transverse. However, the first kinds are not allowed in incompressible fluids, implying that the transverse motions can be described in terms of eddies (chaotic motions in the turbulent flow of fully-developed incompressible turbulence). In this theory viscosity plays no role at larger scales and energy is transferred from larger size eddies to smaller sizes, down to the scale at which viscosity becomes relevant.
For another scenario in which Iroshnikov-Kraichnan turbulence is present in the magnetic field a spectral index $\nu = 3/2$ is expected. This turbulence theory differs from Kolmogorov theory in the explicit assumption of a strong magnetic field, such that the Larmor radius of charged particles is smaller than the size of the eddies.
The different theories describe different rates at which the energy of large eddies dissipate to smaller scale eddies and both provide us with the prediction of a power-law in energy. The identification of these power-laws is a powerful tool to study turbulent fluids and provides clues about the type of turbulence that is present in the fluid.

The diffusion coefficient can be described by a single power-law in rigidity with an effective spectral index δ such that it is linked to the magnetic turbulence spectral index ν via $\delta = \nu - 2$ [22], i.e.

$$K(R) \propto R^{\delta} \qquad \text{where} \qquad \delta = 2 - \nu \tag{26}$$

This means that observation of an effective spectral index $\delta = 1/3$ would indicate Kolmogorov turbulence, while $\delta = 1/2$ would imply Iroshnikov-Kraichnan turbulence.
Given that the injection spectrum of primaries can be parametrised by a single power-law like equation 23 and the diffusion coefficient can be described like equation 26. In a simplified scenario where we only consider sources and diffusion, the density of primaries and secondaries can be described by equations 27 and 28 respectively.

$$n_I \propto \frac{q_I}{K} \propto R^{-\alpha-\delta} \tag{27}$$

$$n_{II} \propto \frac{n_I}{K} \propto \frac{q_I}{K^2} \propto R^{-\alpha-2\delta} \tag{28}$$

$$\frac{n_{II}}{n_I} \propto K^{-1} \propto R^{-\delta} \tag{29}$$

Equations 27 and 28 provide solutions to the diffusion equation (discussed in Section 1.3.1). Combining the two gives an expression for the secondary to primary ratio of CR density for the simplified scenario described above. The expression is given in equation 29. The secondary to primary ratio is only sensitive to propagation effects such as magnetic turbulence, not to the source spectrum. These ratios are therefore a useful tool to investigate CR propagation through the Galaxy.
The fluctuations in the magnetic fields $\delta B/B \ll 1$ that cause spatial diffusion of CRs as described above also cause the CRs to diffuse in momentum space. In other words, the magnetic field fluctuations cause reacceleration of CRs. Momentum diffusion, with its own momentum diffusion coefficient $K_{pp} \equiv \left\langle \frac{\Delta\vec{p}\Delta\vec{p}}{\Delta t} \right\rangle$ [23], is related to spatial diffusion [24] by

$$K(R) \times K_{pp} \approx \frac{1}{9} p^2 V_A^2 \tag{30}$$

where V_A is an effective speed of the magnetic perturbations, comparable to the characteristic speed of magnetohydrodynamic waves, also known as the Alfvénic speed.

In addition to spatial and momentum diffusion, convection can affect the propagation of CRs. Convection of CRs can best be described as mass motion of the plasma away from the galactic disk, outwards into the halo. Similar to the diffusion current for spatial diffusion, we can define the convection current $\vec{j_c} = \vec{V_c} n$ where $\vec{V_c}$ denotes the convective wind velocity. Again combining the current with the continuity equation, this time we obtain a diffusion-convection equation

$$\frac{\partial n}{\partial t} = \vec{\nabla} \cdot (K\vec{\nabla} n - \vec{V_c} n) \tag{31}$$

CR convective winds can escape from the galactic disk. This causes a CR density gradient that creates a pressure gradient. This pressure gradient then generates a force on the ISM [25] and the moment this force overcomes gravity, winds are launched away from the galactic disk [26].

This changes the CR transport through the Galaxy and hence the spectrum we observe. For example, it significantly suppresses the B/C flux ratio at low energies, as can be seen further on in this work in figure 21b.

Collisions with the ISM. Inelastic collisions of primary CRs with the ISM cause the destruction of primary CRs and production of secondary CR species. Secondaries can in their turn interact with the ISM again and produce tertiary CRs, et cetera. Consequently, interaction with the ISM changes the CR flux of various species. In order to describe CRs colliding with the ISM we introduce the destruction (or inelastic) cross-section σ_a of species a producing any secondary species, and the production cross-section $\sigma_{b\to a}$ of species a producing species a from species b by any process. The cross-section can be interpreted as a probability for interaction (here production and destruction) processes to occur. The relation between production and destruction cross-sections is given by

$$\sigma_i^{\text{destruction}} = \sum_{P_k} \sigma_{i\to p_1+p_2+\ldots+p_n} \tag{32}$$

where P_k is the collection of all particles that can be created in the fragmentation of species i.

Radioactive decay of CR nuclei also affects the flux we observe from species, depending on the half-life time of the isotope. If unstable particles reside in the Galaxy for times longer than or comparable to their half-life time, the chance of decaying before interacting with the ISM or a detector becomes significant for these particles. Radioactive decay is thus a process that should be taken into account in the study of CR transport for species with a small half-life time compared to the time a particle resides in the Galaxy. This is relevant especially for Be, which has unstable isotopes, namely ^{10}Be with a half-life of 1.4 My. If ^{10}Be is confined longer in the Galaxy than 1.4 My, the chance of decay is larger than 1/2. Comparison of the abundances of the radioactive isotope and its decay products can provide insights to the propagation time of particles [1]. Lastly we discuss some of the other relevant energy losses that affect the propagation of CR nuclei through the Galaxy. We describe Coulomb losses, ionisation and adiabatic energy losses, starting with the former.

Propagation through the ISM also causes CRs to lose energy by elastic interactions. Nuclei moving through a fully ionised plasma will scatter off thermal electrons as they experience the Coulomb force between two charged particles. The force experienced by particle one is given by

$$\vec{F_1} = \frac{q_1 q_2}{4\pi\epsilon_0} \frac{\vec{r_1} - \vec{r_2}}{|\vec{r_1} - \vec{r_2}|^3} = \frac{q_1 q_2}{4\pi\epsilon_0} \frac{\hat{r_{12}}}{|\vec{r_{12}}|^2} \tag{33}$$

where q_1 and q_2 are the particles charges, $\vec{r_1}$ and $\vec{r_2}$ are the particle locations and $\vec{r_{12}}$ is the distance vector between the particles. The energy loss rate due to Coulomb collisions is given by [27]

$$b_{Coul}(E) \approx -4\pi r_e^2 c m_e c^2 Z^2 n_e \ln\Lambda \frac{\beta^2}{x_m^3 + \beta^3} \tag{34}$$

where x_m and the Coulomb logarithm $\ln\Lambda$ are given by

$$x_m \equiv \left[\frac{3\sqrt{\pi}}{4}\right]^{\frac{1}{3}} \sqrt{\frac{2k_B T_e}{m_e c^2}} \qquad \text{and} \qquad \ln\lambda \approx \frac{1}{2}\ln\left(\frac{m_e^2 c^4}{\pi r_e \hbar^2 c^2 n_e}\frac{M\gamma^2\beta^4}{M+2\gamma m_e}\right) \tag{35}$$

CRs can also lose energy to neutral ISM particles through ionisation. When enough energy is transferred to the electrons, neutral particles can be ionised, causing an ionisation energy loss rate to CRs of [27]

$$b_{ion}(E) = -2\pi r_e^2 c m_e c^2 Z^2 \beta^{-1} \sum_{\text{s=H,He}} n_s B_s \tag{36}$$

where n_s is the density of species present in the ISM and B_s is given by

$$B_s = \left[\ln\left(\frac{2m_e c^2\beta^2\gamma^2 Q_{max}}{\tilde{I_s}^2}\right) - 2\beta^2\right] \tag{37}$$

where the maximum energy transfer to the electron Q_{max} is given by

$$Q_{max} \approx \frac{2m_e\beta^2\gamma c^2}{1+(2\gamma m_e/M)} \tag{38}$$

and $\tilde{I_s}$ denotes the geometric mean of the excitation and ionisation potentials of the targeted atoms.

Finally we consider adibatic losses. In adiabatic treatment of a CR plasma, the particles lose energy as the plasma expands, which gives an adiabatic loss rate of [28]

$$b_{adia}(E) = -\frac{1}{3}(\vec{\nabla}\cdot\vec{V_c})\frac{p^2}{E} \tag{39}$$

Note that bremsstrahlung and compton scattering also causes significant energy losses to CRs. However, this mostly affects positrons and electrons and plays a minor role for nuclei. Hence it does not impact this work significantly and is therefore not discussed in the project.

Figure 7 allows for the comparison of the characteristic timescales of the physical processes involved in the propagation of CRs [29]. In this figure the characteristic timescales of the relevant effects for the propagation of ^{12}C taking place inside the disk are shown as a function of kinetic energy per nucleon. In this visualisation a short timescale corresponds to a dominant propagation process in the corresponding energy domain. The low energy part of the propagation ($E_{k/n} < 1$ GeV/n) is dominated by energy losses with the timescale τ_{losses}. This represents the timescale of Coulomb, ionisation and adiabatic energy losses combined, i.e. $\tau_{losses} = \tau_{coulomb} + \tau_{ionisation} + \tau_{adia}$. The high energy part of the propagation ($E_{k/n} > 2$ GeV/n) is dominated by leakage processes with timescale τ_{leak}. This represents the timescale of diffusion, convection and fragmentation effects combined, i.e. $\tau_{leak} = \tau_{diff} + \tau_{conv} + \tau_{frag}$. The single propagation process that dominates the high energy end is diffusion, at energies $E_{k/n} > 10$ GeV/n.

The last propagation effect that we discuss is the solar modulation. When CRs enter the heliosphere, the region surrounding the Sun and the solar system that is filled by the solar magnetic field, they come across a turbulent solar wind with an embedded heliospheric magnetic field [30]. As a consequence, the energy and intensity of the CRs suffer considerable variations depending on their position in the heliosphere. The time and charge-dependent effects that the solar wind is able to generate significantly affects mainly the intensity of CRs with low energies ($E < 30$ GeV)

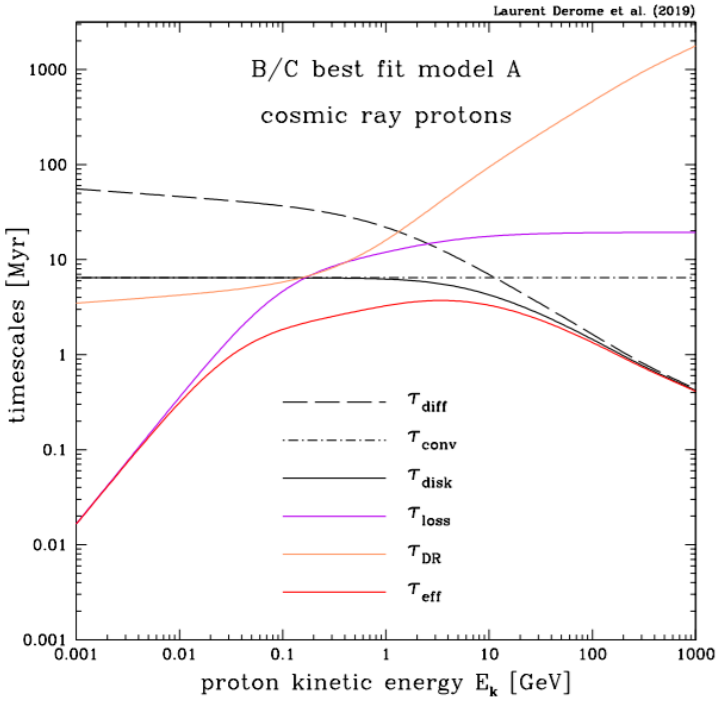

Figure 7: Timescales for various physical processes affecting the propagation of CR nuclei displayed as function of kinetic energy per nucleon. [29]

[30]. To describe this transport effect one can make use of the force-field approximation (FFA) that describes the solar modulation with one single parameter, the solar modulation potential Φ. The energy of unmodulated quantities E^{IS} can be linked [31] to the energy of modulated quantities E^{TOA} via

$$\frac{E^{TOA}}{A} = \frac{E^{IS}}{A} - \frac{|Z|}{A}\Phi. \tag{40}$$

The FFA is consists of four main assumptions: a steady-state system, spherical symmetry, zero streaming (convective and diffusive fluxes cancel out), and a diffusion coefficient that is proportional to rigidity R [32].

1.3.1 The transport equation

The physical processes concerning the acceleration and propagation of CR species in the Galaxy described above can be described mathematically by means of the transport equation.
Cosmic-ray propagation in the Galaxy can be described by [33]:

$$\begin{aligned}\frac{\partial n(\vec{r},p,t)}{\partial t} &+ \vec{\nabla}\cdot(-K\vec{\nabla}n + \vec{V}_c n) \\ &+ \frac{\partial}{\partial p}\left[\dot{p}n + \frac{p}{3}(\vec{\nabla}\cdot\vec{V}_c n)\right] - \frac{\partial}{\partial p}p^2 K_{pp}\frac{\partial}{\partial p}\frac{1}{p^2}n \\ &= \text{Source}(\vec{r},p,t) - \text{Sink}(\vec{r},p,t)\end{aligned} \tag{41}$$

where $n(\vec{r},p,t)$ is the CR density per particle momentum p, K is the spatial diffusion coefficient, $\vec{V}_c$ is the convection velocity, $\dot{p} \equiv dp/dt$ are the particle momentum losses and K_{pp} is the

momentum diffusion coefficient that describes reacceleration. The equation is a combination of the continuity equation (first line), the energy current (second line) and source and sink terms. Various source and sink terms are described below.

Source terms

Cosmic rays of primary origin are those that originate from diffusive shock acceleration, which is considered to be the dominant mechanism to accelerate all species. This can occur in supernova remnants (see Section 1.1). The injection spectrum can be described by a power-law $R^{-\alpha}$ where R is the rigidity and α is the source spectral index. CRs of primary origin are called *primaries* for short.
Cosmic rays of secondary origin are those that originate from interactions of primary CRs with the ISM resulting in the creation of secondary particles (e^+,e^-,γ,ν), anti-nuclei and secondary nuclei such as Li, Be and B, which are fragments of heavier CR nuclei. These CRs are called *secondaries*.
Secondary CRs can in their turn interact inelastically with other particles without annihilating. This causes a redistribution of particles in energy as the interacting particles with high initial energy lose part of their energy to the interacting particles with low initial energy. The resulting particles are called cosmic rays of tertiary origin and nicknamed *tertiaries*.
Cosmic rays of radioactive origin also enter the transport equation through source terms as they are a source of new CRs after the decay of their parent species.

Sink terms

Inelastic interactions with the ISM lead to the destruction of CRs, that hence do not propagate any further, resulting in a sink term in the diffusion equation. Heavy nuclei are affected than lighter nuclei more by this process, because cross-sections scale with $A^{2/3}$ [33].
CRs can interact inelastically with other particles. This causes a redistribution of particles in energy as the interacting particles with high initial energy lose part of their energy to the interacting particles with low initial energy. The particles are not observed with their original energies before interacting inelastically and therefore they enter the diffusion equation in the redistribution sink term.
When CR nuclei are radioactively unstable, they can decay to smaller species. The parent species are removed from transport through the Galaxy and therefore appear in the diffusion equation in a sink term.

1.4 Measurements of galactic cosmic rays with the AMS-02 experiment

The unprecedented percent precision measurement of the current generation space-based experiments, such as Fermi-LAT, PAMELA, CREAM and the AMS-02 detector, revealed unexpected features in galactic CR fluxes. A spectral index transition is observed in the fluxes of primary and secondary CR species above 200 GeV, and substantial evidence points towards a diffusive origin for this feature. In the following we will describe most of the data relevant to this project, collected by the Alpha Magnetic Spectrometer (AMS). This is a state of the art particle detector taking data on the International Space Station (ISS) since 2011. Among the science goals were the studies of the precise origin of Dark Matter (DM), antimatter and CRs, but also to explore new phenomena. This device, AMS-02, detects particles amongst which nuclei from H to Fe, anti-protons, electrons and positrons at unprecedented accuracy. AMS-02 provides accurate, precise CR flux spectra at the GV - TV rigidity range.

The AMS-02 detector consists of various elements[1]. AMS is equipped with a permanent magnet that produces a magnetic field of 1.4 kG at the magnet center and causes negligible dipole moment and field leakage outside the magnet. At the top of the AMS-02 detector a Transition Radiation Detector (TRD) is located. This detector identifies electrons and positrons by their transition radiation. It also distinguishes nuclei by their rate of energy loss dE/dx. Particle detections are triggered by the Time of Flight counters. These counters measure the velocity and direction of incoming particles. Moreover, the TOF measure their charge via the energy losses dE/dX. The Anticoincidence counters (ACC), also called veto counters, exclude particles that enter or exit the tracker volume traversely. Velocity and charge of incoming particles are measured by a Ring Imaging Cherenkov counter (RICH). The final device that makes up the AMS-02 detector is the Electromagnetic Calorimeter (ECAL), an important instrument for the detection and measurement of the energy of electrons and positrons. This device is located at the bottom of AMS-02. A schematic view of the AMS-02 detector can be found in Figure 8.

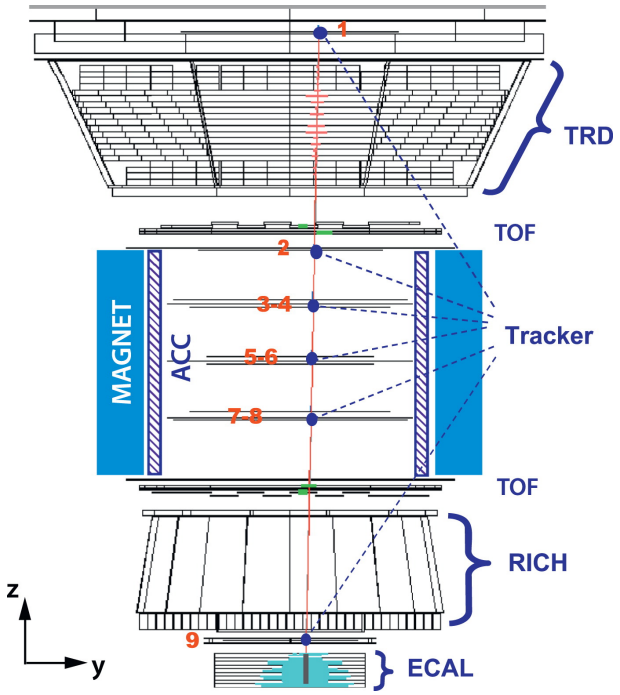

Figure 8: Schematic view of AMS-02 detector present on the International Space Station. [34]

1.4.1 Measurement of primary cosmic-ray species

Protons are the most abundant species of charged CRs and the H flux measured by AMS-02 together with other recent measurements was already shown in Figure 1. This figure displays the unprecedented precision detection of the AMS-02 experiment. The precise proton flux between 1 GV and 1800 GV is based on 1 billion protons detected by AMS from May 2011 till May 2018. Figure 9 allows for investigation of the AMS proton flux and shows the deviation from a single power-law, as is the case for He, C and O. The upper panel displays the proton flux AMS-02 data points in red, together with a single power-law with a constant spectral index γ

$$\Phi = CR^{\gamma} \tag{42}$$

where C is a constant (dotted line). We can see clearly that the measurements do not fit the single power-law at rigidities above 45 GV.

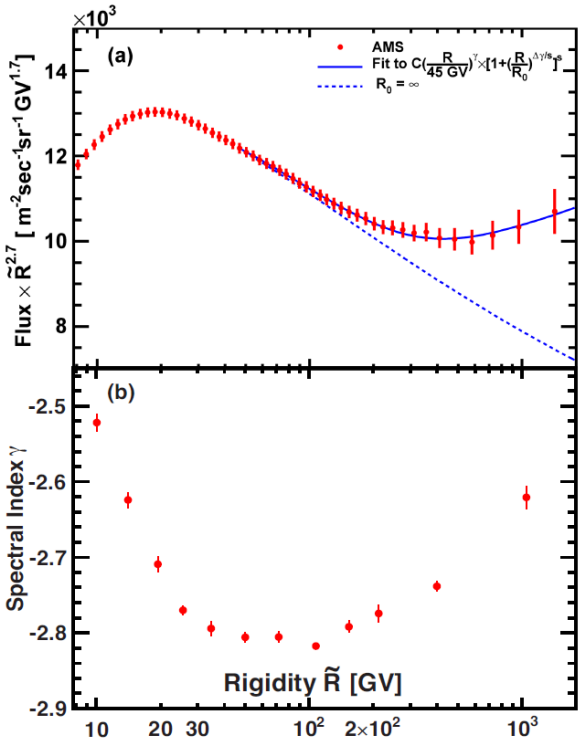

Figure 9: Rigidity dependence of the H flux (upper panel) and the H flux spectral index (lower panel) measured by AMS-02. [1]

Given the high precision of AMS-02 data, it is possible to perform detailed studies of the individual CR spectra. In particular, it is for the first time possible to study the rigidity dependence of the flux spectral index γ:

$$\gamma = \frac{d[\log(\Phi)]}{d[\log(R)]} \tag{43}$$

This quantity shows how much spectrum deviates from a single power-law. When the flux spectral index does not vary as a function of rigidity, i.e. $\gamma = constant$, the flux follows a single power-law as a function of rigidity. Figure 9 shows that this is not the case for CR protons. The lower panel of the figure shows the H flux spectral index as a function of rigidity and we find that the flux spectral index is hardening [1] at higher rigidities.

For over 30 years the most abundant primaries, i.e. hydrogen, helium, carbon and oxygen, have been studied by use of balloon flight experiments, satellites. Despite the large uncertainties on the measurements of the experiments observing He, C, and O (over 15% at 50 GeV/n) the data obtained from the different experiments are not always consistent with each other.
This has changed with the AMS-02 experiment. AMS provides accurate, precise CR flux spectra at the GV - TV rigidity range. The flux measurements are obtained from the detection of 125

[1] Hardening is the increase of a spectral index. The opposite is called softening and corresponds to the decrease of a spectral index.

million helium, 14 million carbon and 12 million oxygen nuclei from May 2011 till May 2018. The large amount of detected events leads to uncertainties of ∼3% at 100 GV for carbon and oxygen flux data and only ∼1.5% at 100 GV on helium flux. Figure 10 displays the improvement made by AMS-02 regarding CR spectra of the primary species helium, carbon and oxygen. The figure also shows that the three spectra have identical rigidity dependence. Especially above 200 GV, where they all deviate from the single power-law and harden progressively.

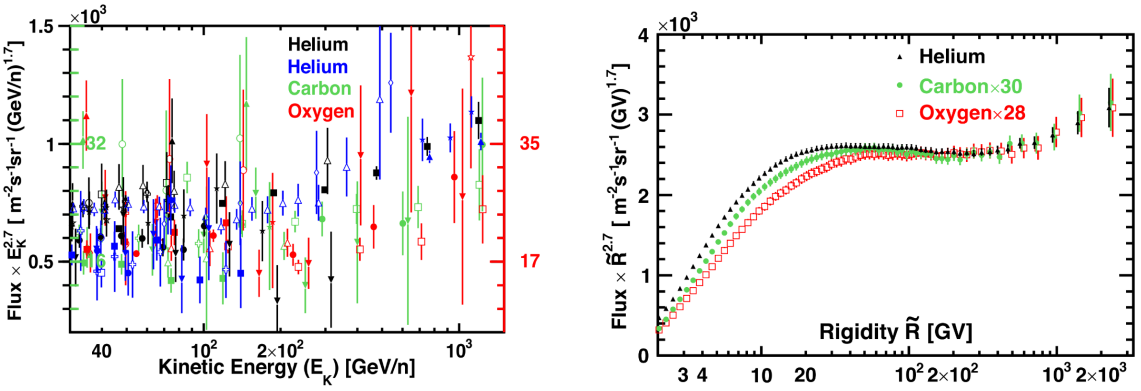

(a) (b)

Figure 10: Comparison of flux measurements of primary cosmic rays He, C and O (a) before AMS-02 and (b) from AMS-02. [1]

Figure 11a shows the flux spectral index of primaries He, C and O. The rigidity dependence is similar above 60 GV for all three primaries. Moreover, the flux spectral index is hardening and shows identical behavior above 200 GV for all three species. The identical behavior of the flux at high rigidity is visualised more clearly in Figure 11b.

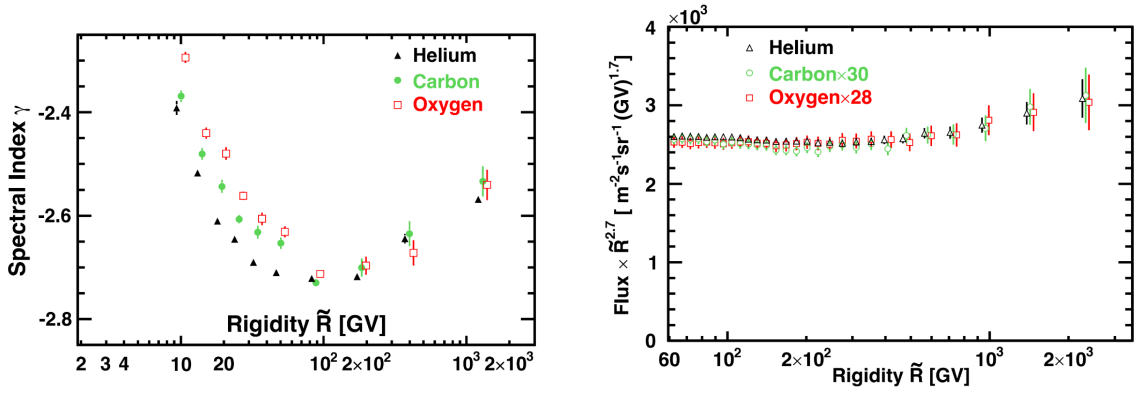

(a) (b)

Figure 11: Rigidity dependence of (a) flux spectral index of He, C and O and (b) flux of He, C and O, measured by AMS-02. [1]

1.4.2 Measurement of secondary cosmic-ray species

As discussed in Section 1.3.1, interactions of primary CRs with the ISM result in the creation of secondary CRs. Lithium, beryllium and boron are believed to be purely of secondary origin. Precise spectra of secondaries at the GV-TV rigidity range can provide important information on

the propagation of CRs through the ISM. It also provides an opportunity to study the properties of the ISM. Before AMS, only a small amount of experiments have measured the fluxes of these species in the GV - TV rigidity range. Typical uncertainties on the flux measurement in these experiments are larger than 50% at 100 GV for lithium and beryllium. The measurements in these pre AMS experiments on the boron flux have typical uncertainties larger than 15%. Figure 12 shows the lithium, beryllium and boron flux measured by experiments before AMS.

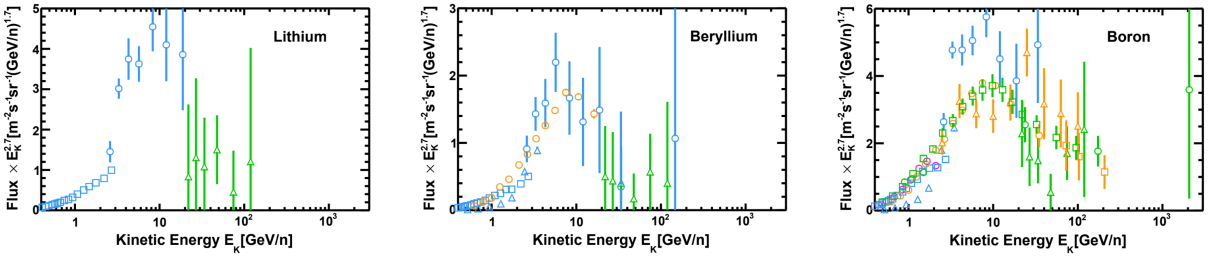

(a) (b) (c)

Figure 12: Flux measurements of secondaries before AMS-02 of (a) lithium, (b) Beryllium and (c) boron, measured by AMS-02. [1]

The AMS-02 experiment provides accurate, precise lithium, beryllium and boron flux spectra at the GV - TV rigidity range. The flux measurements are obtained from the detection of 3.0 million lithium, 1.7 million beryllium and 4.2 million boron nuclei from May 2011 till May 2018. The large amount of detected events leads to uncertainties of ∼3% at 100 GV for all three species. Figure 13 shows the lithium, beryllium and boron flux measured by AMS-02. A comparison of Figure 12 and Figure 13 visualises the improvement made by AMS-02.

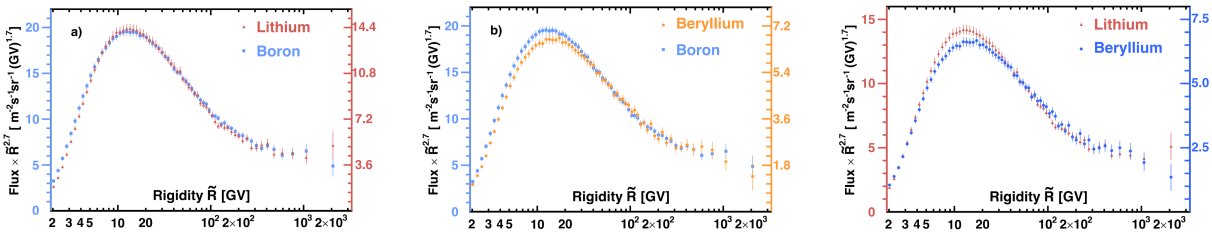

(a) (b) (c)

Figure 13: Flux measurements of secondaries before AMS-02 of (a) lithium and boron, (b) beryllium and boron, and (c) lithium and beryllium. [1]

Figure 13 shows identical rigidity dependence of lithium boron fluxes above ∼ 7 GV. Above ∼ 30 GV the rigidity dependence of the fluxes of all three secondary species is identical. Below ∼ 30 GV the flux differences of beryllium and the other two species is most likely due to the radioactive nature of the ^{10}Be isotope. At low rigidity the half-life of $1.4 \cdot 10^6$ y causes these isotopes to decay before they arrive at the detectors.

Analogously to the calculation of the flux spectral index γ for primaries in Section 1.4.1, we can calculate the flux spectral index for the secondaries using equation 43. Primaries helium, carbon and oxygen showed progressive hardening in the spectrum above ∼ 200 GV. In order to investigate the origin of the hardening, the hardening of primaries can be compared to the behavior of the spectral flux index of secondaries. This can give insight about the origin of this

hardening, and whether it is due to phenomena occurring at the sources or during the propagation. Figure 14 shows the flux spectral index as a function of rigidity for both primaries helium, carbon and boron (grey) and secondaries lithium, beryllium and boron (blue). Similar to the primaries, the secondaries show a nearly identical rigidity dependence. However, the rigidity dependence of the secondaries is significantly different from that of the primaries. The secondaries appear to show even more hardening than the primaries above $\sim$ 200 GV.

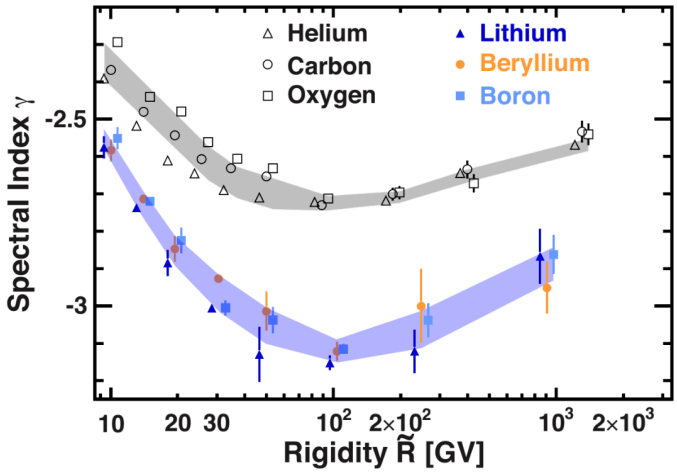

Figure 14: Rigidity dependence of the flux spectral index of primaries He, C and O, and secondaries Li, Be and B. The grey and blue regions, for primaries and secondaries respectively, are present to guide the eye. [1]

1.4.3 Measurement of secondary to primary ratios of cosmic-ray species

Figure 15 shows the ratios of lithium, beryllium and boron fluxes to the carbon flux.

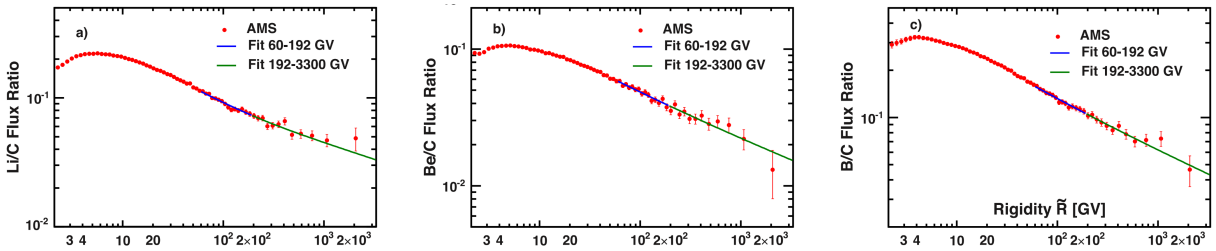

(a) (b) (c)

Figure 15: Primary to secondary ratio spectra fitted with a single power-law $\frac{\Phi_S}{\Phi_P} \propto R^{\delta}$ on two non-overlapping intervals for (a) Li/C, (b) Be/C and (c) B/C . [1]

The ratios are fitted with a single power-law function

$$\frac{\Phi_S}{\Phi_P} \propto R^{\Delta} \tag{44}$$

where Φ_S and Φ_P stand for the fluxes of secondaries and primaries, respectively. The fits are performed over two separate rigidity ranges, 60 - 192 GV and 192 - 3300 GV. The obtained average hardening is found to be

$$\Delta_{[192-3300]\mathrm{GV}} - \Delta_{[60-192]\mathrm{GV}} = 0.140 \pm 0.025$$

The hardening present in the spectra of the flux ratios shows that the secondaries are hardening more than the primaries. This is visualised more clearly in Figure 16. The significance of this hardening is found to be larger than 5σ by the AMS collaboration [1]. The finding that secondary CRs harden more than primary CRs is an indication that hardening is due to the propagation of CRs through the Galaxy. If the hardening would be the result of a source effect, this would be appearing in the spectra of both primary and secondary species, and the secondary to primary ratio would appear featureless. In the next chapters we will investigate the propagation of CRs by studying secondary to primary ratios with the help of semi-analytic models.

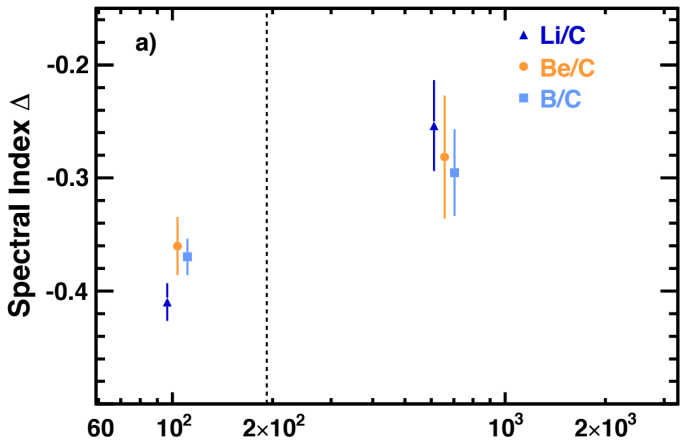

Figure 16: Spectral index of secondary to primary ratios (Δ) of Li/C, Be/C and B/C as function of rigidity, meansured by AMS-02. [1]

2 Analysis of cosmic-ray transport with semi-analytical models

This section describes the methods that we have used in this project. We have studied the CR transport using the USINE code, which provides a framework to solve the transport equation semi-analytically. First we describe the general use of semi-analytical models (SAMs) in the study of CR transport. Later we describe three benchmark models for the CR propagation that have been derived in the literature from the analysis of the recent B/C data. Finally we show the impact of the variation of several model parameters on the B/C flux ratio.

2.1 Semi-analytical approach

For the purpose of studying CR transport from their source through the Galaxy to our detector, solving the diffusion equation (equation 41) is essential: this cannot be done fully analytically, hence one has the choice either to use fully numerical simulations or SAMs. The former is a very accurate method that can include all the physics the user inserts in the model, at the expenses of a large computational cost. For the latter method one makes use of assumptions and approximations, such as simplified geometry or simplified description of the physical processes considered in the calculations, such as diffusion, convection and energy gains and losses. The main advantage of using these SAMs is that solving spatial derivatives analytically is computationally not very expensive, allowing for fast simulations compared to numerical models.
The USINE package [33] can be used to solve the CR transport equation in a semi-analytical fashion. In this way standard analysis methods such as Green functions, Fourier transforms and Bessel functions can be used to solve spatial derivatives or momentum derivatives. Some of the models included in the USINE software are outlined below. The Leaky Box model assumes a steady-state, no spatial dependence of CR density, diffusion or convection, homogeneous distribution of gas and homogeneous distribution of CR sources. The model contains three free parameters: the density of the various elements n_i [cm^{-3}], the escape length $\lambda_{esc}(E)$ [g cm^{-2}] and the pseudo-Alfvénic speed of scatterers for reacceleration $\mathcal{V}_A$ [km s^{-1} kpc^{-1}]. The 1D diffusion model assumes a steady-state, 1D geometry (i.e. the Galaxy is described as a radially infinite slab), homogeneous distribution of gas and sources, isotropic and spatial-independent diffusion, reacceleration and constant wind. The model contains seven free parameters: the density of the various elements n_i [cm^{-3}], spatial diffusion coefficient $K(E)$ [kpc^2 Myr^{-1}], momentum diffusion coefficient $K_{pp}(E)$ [GeV^2 Myr^{-1}], Alfvénic speed V_A [km s^{-1}], constant velocity V_c[km s^{-1}], diffusive halo half-height L [kpc] and the size of local underdense region r_h [kpc]. The 2D diffusion model deviates from the 1D diffusion model as it assumes a 2D geometry, i.e. the Galaxy can be described as a 2D cylindrical box, adding the radius of the cylindrical box R [kpc] as an additional parameter. Users of USINE can also modify these models to their wishes or define new models and use them to, amongst others, generate CR fluxes based on various models, fit model parameters to data, generate comparison plots and obtain plots of fractional components of elements.

2.2 The 1D diffusion model

In the 1D diffusion model the Galaxy is described by a thin disk of half-height $2h$ embedded in a cylindrical diffusive halo of half-height L. The thin disk represents the relatively dense disk in the Galaxy that consists of dense gas, dust and stellar mass. The halo stands the large magnetic halo of the Galaxy in which the disk is embedded. In reality the thickness of the galactic disk is two orders of magnitude smaller than the size of the magnetic halo, i.e. $h \ll L$. This allows us to treat the disk to be an infinite thin disk embedded in the halo. The gas density in the

halo is considered to be negligible. As well in the halo as in the disk, CRs diffuse independently of position. The propagation of high energy CRs is highly diffusive. However, the impact of convection cannot be neglected. Therefore we consider a constant convective wind with speed V_c in the galactic halo. The simplification of the geometry of the Galaxy is visualised in Figure 17. The parameters L, h and V_c are pointed along $\hat{\boldsymbol{z}}$, perpendicular to the thin disk.

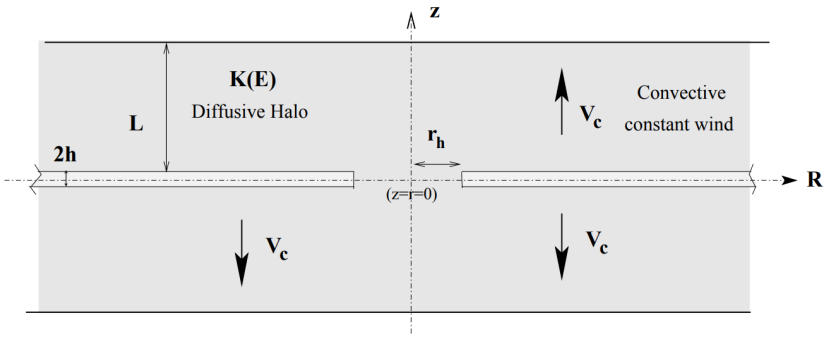

Figure 17: Sketch of the galaxy in the Standard 1D diffusion model [28].

2.2.1 Assumptions

The assumptions on which the 1D diffusion model is based are listed below [33]:

- Steady-state
- 1D geometry: a thin disk of half-height h and a diffusive halo of half-height L
- Homogeneous distribution of galactic CR sources and gas
- Spatially independent and isotropic diffusion of CRs in the thin disk and the diffusive halo
- Reacceleration occurs only in the thin disk, due to interactions of CRs with charged particle plasmas in the ISM
- Constant convective wind in the halo implying a discontinuity

2.2.2 Free Parameters

The 1D diffusion model contains seven free parameters that are listed below [33]:

- n_i [cm^{-3}]: the density of various elements in the thin disk
- $K(E)$ [$\mathrm{kpc}^2\,\mathrm{Myr}^{-1}$]: the isotropic and homogeneous spatial diffusion coefficient
- $K_{pp}(E)$ [$\mathrm{GeV}^2\,\mathrm{Myr}^{-1}$]: the momentum diffusion coefficient in the thin disk
- V_A [$\mathrm{km\,s}^{-1}$]: the Alfvénic speed for reacceleration in the thin disk
- V_c [$\mathrm{km\,s}^{-1}$]: the constant velocity of convective winds in the halo
- L [kpc]: the half-height of the diffusive halo

2.3 Benchmark models

The diffusion coefficient is an important ingredient and it is assumed to be a scalar function of the CR rigidity, homogeneous and isotropic over the whole magnetic halo. The diffusion coefficient describes the CRs scattering off magnetic turbulence. As stated in Section 1.3, the rigidity

dependence of the diffusion coefficient should follow a simple power-law $K(R) \propto R^{\delta}$ where $\delta = 2 - \nu$ is related to the magnetic turbulence spectrum power-law index $(\delta B/B) \propto k^{\nu}$ [2, 20, 21].

$$K(R) = \beta^{\eta_t} K_0 \left\{ 1 + \left(\frac{R}{R_l} \right)^{\frac{\delta_l - \delta}{s_l}} \right\}^{s_l} \left\{ \frac{R}{(R_0 \equiv 1 \text{ GV})} \right\}^{\delta} \left\{ 1 + \left(\frac{R}{R_h} \right)^{\frac{\delta_h}{s_h}} \right\}^{-s_h} \tag{45}$$

The first evidence for a break in the B/C was found by AMS-02 [8, 9]. This break most probably originates from a transition of diffusion regime rather than from source effects [10, 35]. Following the approach presented in [35], the diffusion coefficient (Equation 45) includes a break in both the low- and high-rigidity range. In this equation, R_l and R_l represent the rigidity scales of the low- and high-rigidity breaks, respectively. Parameters δ_l and δ_h are the power-law indices of the low and high rigidity breaks, respectively. The smoothness parameters of the rigidity breaks are named s_l and s_h. These are introduced to describe the smooth transition in the spectral index observed in all AMS-02 fluxes above 200 GV. Equation 45 also describes the non-relativistic regime by means of the non-relativistic parameter $\beta = v/c$, the dimensionless speed of the CR particles. Non-relativistic processes in the low rigidity regime can be accounted by raising β to the power η_t, which is an effective parameter. K_0 is the normalisation parameter taken at $R_0 = 1$ GV.[2] The physical process responsible for the spatial diffusion of CRs is the scattering off plasma waves. This process also causes reacceleration of CRs, i.e. diffusion in momentum. This can be accounted for by the diffusion coefficient in momentum space K_{pp}, described by Equation 46.

$$K_{pp}\ [\text{GeV}^2\,\text{Myr}^{-1}] = \frac{4}{3} V_A^2 \beta^2 E^2 \frac{1}{\delta(4-\delta^2)(4-\delta) K(R)} \tag{46}$$

The diffusion coefficient in momentum space is directly related to the spatial diffusion coefficient. It also depends on δ, the diffusion spectral index that describes the intermediate rigidity regime. Moreover, we introduced the (effective) Alfvénic speed V_A. This is the speed of the plasma waves and characterises the magnetic turbulence.
Lastly, we include convection in CR propagation models as a consequence of the global motion of the plasma. Convection is often parametrised in a standard way, in which convective winds of constant speed V_c are pointed along the vertical coordinate in the 1D diffusion model. V_c is positive above the thin disk and negative below. This can be seen in Figure 17 and Equation 47.

$$\vec{V_c}(z) = \frac{z}{|z|} V_c \hat{\mathbf{z}} \tag{47}$$

We make use of the three propagation models, dubbed BIG, SLIM, and QUAINT, which were proposed in [35]. These models were found to provide an accurate description of the B/C data from AMS-02 and individual fluxes of Li, Be, B, and the helium isotopes [36], as can be seen in Figure 18.

The BIG model is the most generic model and contains a diffusion coefficient with a double rigidity break as described in Equation 45. The diffusion coefficient also includes the non-relativistic parameter η_t. In one case this parameter can be fixed to $\eta_t = 1$ while in other cases it may be allowed to vary. The BIG model also includes reacceleration and convection.

[2] Note that in literature normalisation parameters are taken at this rigidity, or other rigidities like $R_{10} = 10$ GV (e.g. [35]). The corresponding normalisation parameter K_{10} cannot be directly compared with K_0 and should be first be converted. This can be done using $K_{10} = K_0 \cdot 10^{\delta}$ or equivalently, by making use of the relation $\log_{10}(K_{10}) = \log_{10}(K_0) + \delta$.

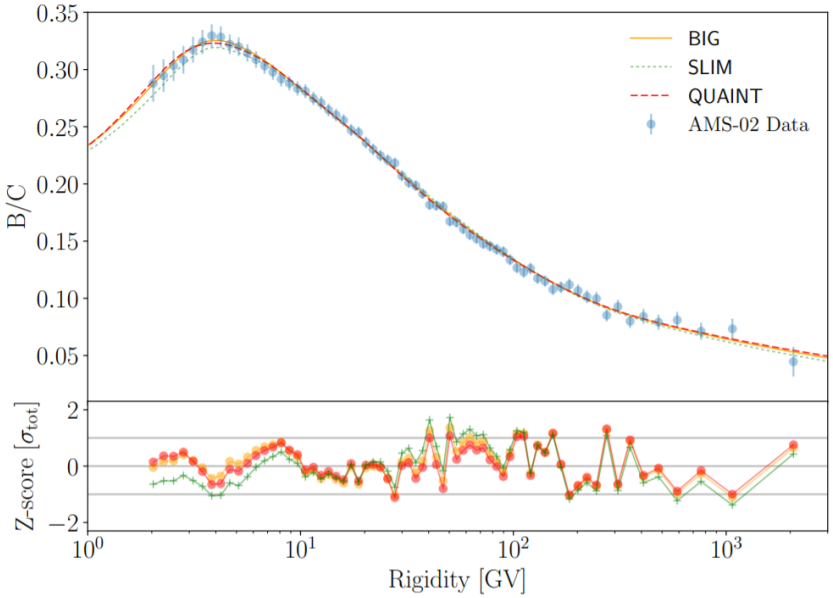

Figure 18: Best fit B/C curve for models BIG, SLIM, and QUAINT. The bottom panel shows the Z-score. [35]

The SLIM model is a limiting case of the BIG model. It takes neither reacceleration nor convection into account, i.e. $V_A = 0$ km s^{-1} and $V_c = 0$ km s^{-1} respectively.[3] This model also does not allow the non-relativistic parameter to vary and fixes it at unity, i.e. $\eta_t = 1$. This makes the SLIM model much less flexible compared to the BIG model and forces the CR spectral features to be described by parameters related to magnetic turbulence features.

Another limiting case of the BIG model is called QUAINT. Contrary to the SLIM model, QUAINT does take reacceleration, convection and the non-relativistic parameter into account, i.e. it allows V_A, V_c and η_t to vary. Instead, it discards the high and low-rigidity breaks as free fit parameters. This model originates from earlier astrophysical models described by parameters giving the maximal, median, and minimal supersymmetric antiproton flux and compatible with B/C analysis [37]. The three benchmark models are summarised in Table 1.

2.4 Impact of parameter variation on the B/C flux ratio

To investigate the behavior of various parameters as function of rigidity, we make use of the USINE software. We take parameter values from [38] (Table 2) to draw a B/C flux ratio (Φ_{BC}) using a SLIM model. The parameter values are obtained from the combined analysis of Li/C, Be/C and B/C flux ratios and provide an accurate discription of the B/C flux ratio as can be seen in Figure 19. The figure shows Φ_{BC} generated by USINE together with the AMS-02 measurements of the B/C flux ratio for which the total uncertainties are shown.

With the SLIM model and the parameter values from [38] (Table 2) we can also draw fluxes and flux ratios for other species and compare them to the AMS-02 measurements. The results of these simulations can be found in Appendix A, in Figure A.1 which shows the fluxes, and Figure A.2 which shows the flux ratios.

The flux obtained simulations with the SLIM model and parameter values taken from [38] is

[3] Note that for numerical stability these parameters are sometimes fixed at a very small, but non-zero value in minimisation software.

Parameters	BIG	SLIM	QUAINT
Low-rigidity parameters			
V_A [km s^{-1}]	YES	NO	YES
V_c [km s^{-1}]	YES	NO	YES
η_t	YES	NO	YES
R_l [GV]	YES	YES	NO
δ_l	YES	YES	NO
s_l	YES	YES	NO
Intermediate-rigidity parameters			
K_0 [kpc^2 Myr^{-1}]	YES	YES	YES
δ	YES	YES	YES
High-rigidity break parameters			
R_h [GV]	YES	YES	YES
δ_h	YES	YES	YES
s_h	YES	YES	YES

Table 1: Overview of parameters included in BIG, SLIM and QUAINT.

considered the base flux realisation close to the B/C flux ratio observed by AMS-02. In addition to this, we draw flux ratios with model parameter values at the lower and upper boundaries of the range of reasonably realistic values. We do this for model parameters α, Φ, V_a, V_c, δ, L, and K_0.

Figures 20a and 20b illustrate the rigidity dependence of the B/C flux ratio generated with the USINE software for various source spectral index (α) and solar modulation (Φ) values, respectively. From equation 29 we would expect a secondary to primary ratio like B/C to be insensitive to the source spectral index. However, for the extreme cases in which $\alpha = 3$ and $\alpha = 1.5$ we do observe an observable difference of $\sim$11% on the GV-TV rigidity range. Although this effect is only slim for extreme scenarios, it is not negligible and we consider α as nuisance parameter in minimisation procedures. We also do not expect the solar modulation potential to influence the B/C flux ratio significantly due to the comparable Z/A ratio of the B and C isotopes. Equation 40 predicts B and C to be affected similarly by the solar modulation effect for the most abundant isotopes ^{10}B, ^{11}B, ^{12}C and ^{13}C, which all have Z/A in the range 0.45-0.5. Figure 20b confirms this prediction and shows that the B/C flux ratio is only affected by solar modulation at $R < 10$ GV. This parameter is also included as nuisance parameter in fitting procedures.

Parameter [unit]	Value
α [-]	2.362
Φ [GV]	0.79
V_a [km s^{-1}]	7
V_c [km s^{-1}]	0
δ [-]	0.51
L [kpc]	5
K_0 [kpc^2 Myr^{-1}]	0.039

Table 2: Model parameter values taken from [38].

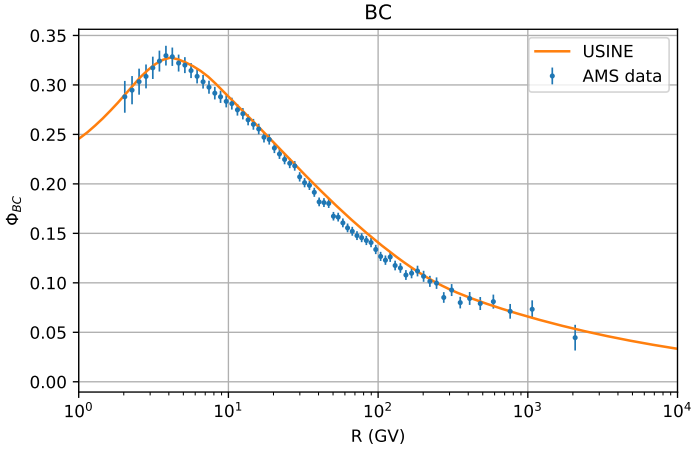

Figure 19: B/C flux ratio Φ_{BC} generated by USINE together with the AMS-02 measurements of the B/C flux ratio. For AMS-02 data we display the total uncertainty, given by the statistical and systematic uncertainty summed in quadrature.

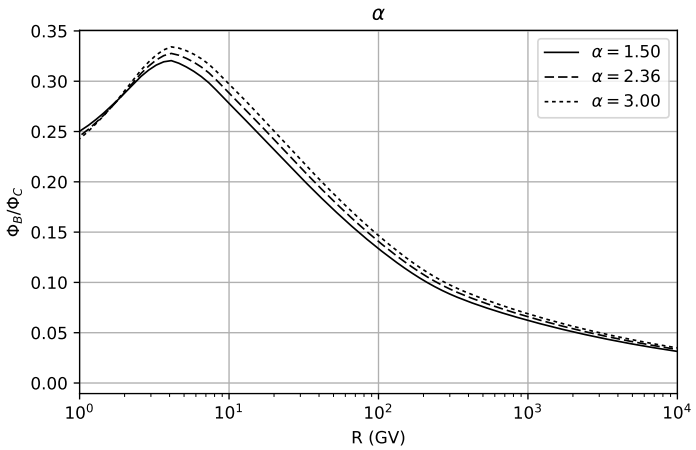

(a)

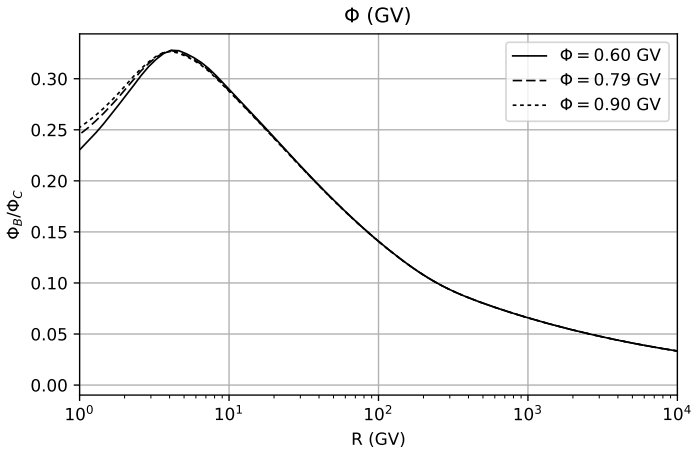

(b)

Figure 20: Flux ratio realisations drawn with the use of USINE for various values of the source spectral index α and solar modulation parameter Φ.

Figures 21a and 21b illustrate the rigidity dependence of the B/C flux ratio generated with the USINE software for various characteristic reacceleration speed (V_a) and convection speed (V_c) values, respectively. Note that because the best fit value obtained by [38] coincides with an extreme value (0 $\mathrm{km\,s^{-1}}$) we cannot take a value lower than this. Therefore, we take a high and middle value for V_c to illustrate the impact of this parameter on the B/C flux ratio. We observe that both the characteristic reacceleration speed and the convection speed impact the secondary to primary B/C flux ratio significantly at low rigidity.

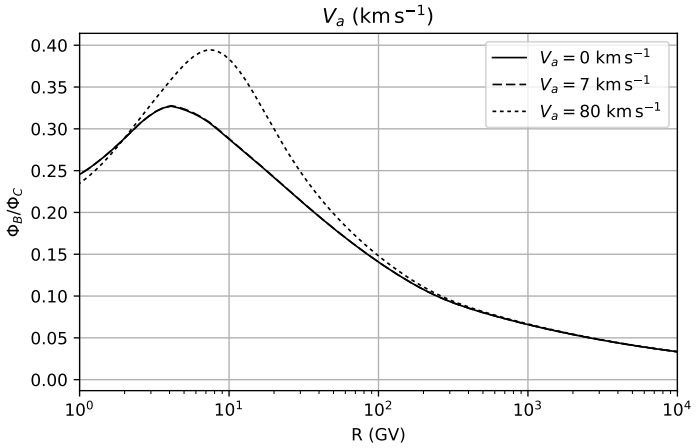

(a)

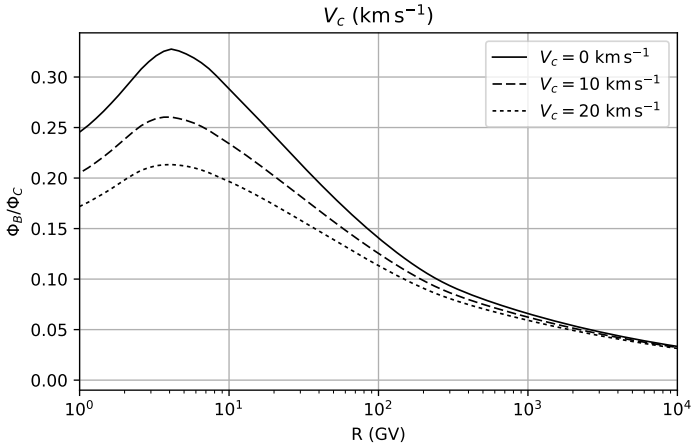

(b)

Figure 21: Flux ratio realisations drawn with the use of USINE for various values of the characteristic reacceleration speed V_a and convection speed V_c.

Figures 22a, 22b and 22c illustrate the rigidity dependence of the B/C flux ratio generated with the USINE software for various effective spectral index values (δ), diffusive halo half-height values (L) values and diffusion coefficient normalisation values (K_0), respectively. All three parameters have significant impact on the secondary to primary B/C flux ratio, indicating that all three parameters are important in the transport of CRs. One feature that stands out, is that an increase of L impacts the flux ratio similar as a decrease of K_0 and vice versa. The correlation is in fact so strong that a scaling relation between the diffusion coefficient normalisation and

diffusive halo half-height still holds with accurate AMS-02 data and is found to be $\frac{K_{10}}{L} \sim 0.3$ [35]. For this reason, variation of L only leads to a rescaling of the normalisation of the diffusion coefficient. L is therefore often fixed to 5 or 10 kpc (e.g. [24, 29, 38]).

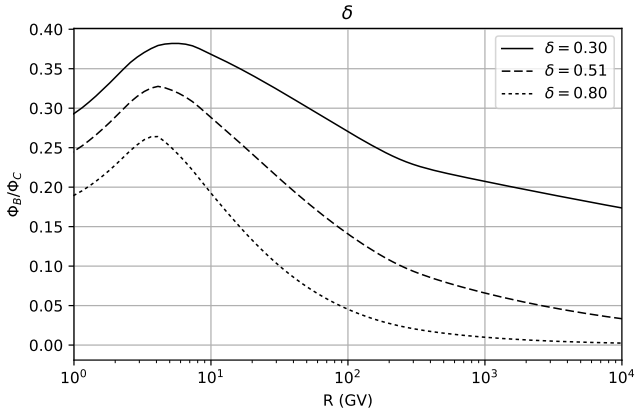

(a)

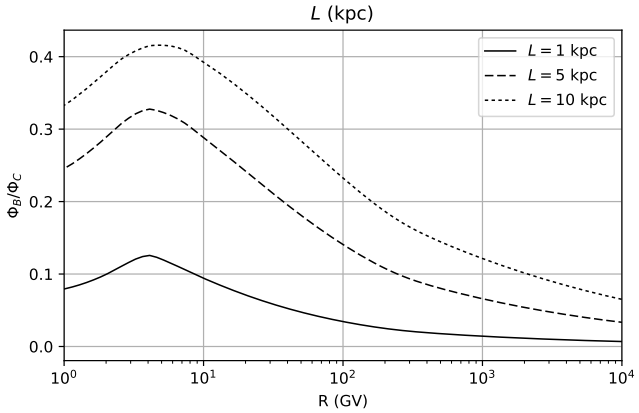

(b)

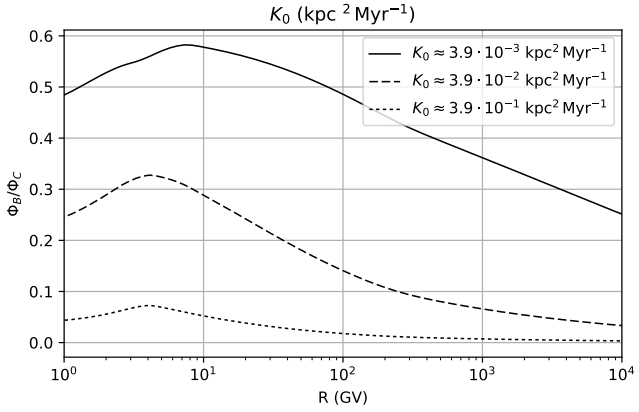

(c)

Figure 22: Flux ratio realisations drawn with the use of USINE for various values of the effective spectral index δ, diffusive halo half-height values (L) values and diffusion coefficient normalisation values (K_0).

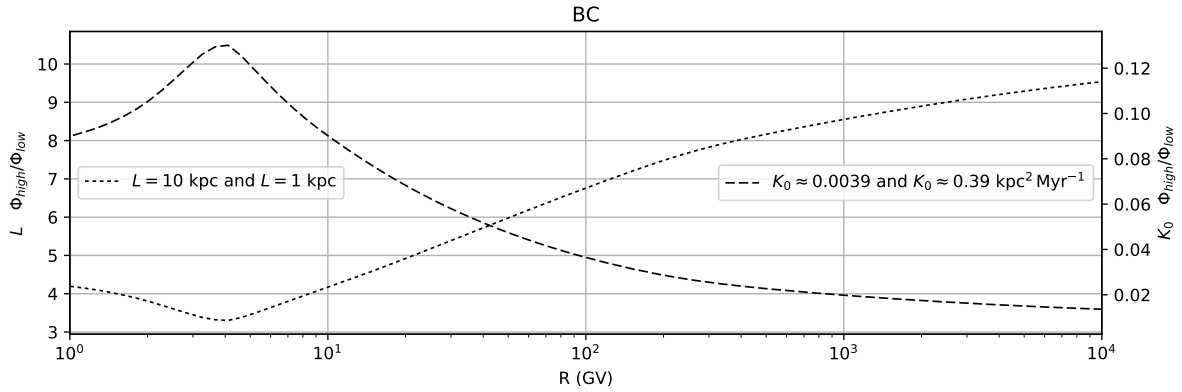

Figure 23: Opposite impact on the B/C flux ratio of the variation of parameters L and K_0 as function of rigidity. The left axis shows the effect of the increase of L, i.e. $\frac{\Phi_{L,high}}{\Phi_{L,high}}$. The right axis shows the effect of the increase of K_0, i.e. $\frac{\Phi_{K_0,high}}{\Phi_{K_0,high}}$

3 Methodology and results of B/C analysis

The literature widely accepted [39] that the description of the CR interactions plays a crucial role in the robustness of the constraints derived from the interpretation of the latest data. In this wor, we follow the method presented in [29] and study the effect of cross-sections on the determination of propagation parameters. We generate mock data based on the B/C data from the AMS-02 experiment, and perform a statistical analysis of the mock data. The following outlines the mock data generation and fitting procedure for various configurations of different models and cross-section parametrisations.

3.1 Cross-section parametrisations

Nuclear cross-sections are measured in experiments not directly related to CR physics. The parametrisations of nuclear cross-sections rely on different approaches, such as inspection of observed properties of nuclear fragmentation [39]. Other parametrisations rely on regularities observed for certain mass differences between the fragments and the parent nucleus, and the ratio of the number of neutrons and protons in the fragments [39]. Another approach is the inspection of the quality and systematics of various datasets and semiempirical formulae [39]. The parametrisations of nuclear cross-sections do not always agree with one another within uncertainties. Fitting procedures therefore benefit from the inclusion of cross-section nuisance parameters compatible with various cross-section parametrisations. Nuisance parameters are parameters that are not of interest in the model, but do influence the analysis. Examples of such nuisance parameters are the solar modulation parameter Φ and CR cross-section parameters σ_{prod}, σ_{inel}. The values and corresponding uncertainties of CR cross-sections are determined in 'external' experiments and affect the minimisation procedure and outcome of transport model parameters [29]. Two ways to include cross-section parameters are described below.

3.1.1 Normalisation, scale and slope (NSS)

One way to include nuisance parameters for nuclear cross-sections compatible with multiple cross-section parametrisations is to start from one reference cross-section parametrisation and apply simple transformations on it [29]:

$$\text{– Normalisation :} \qquad \sigma \to \sigma \times \text{Norm.} \tag{48}$$

$$\text{– Scale :} \qquad E_{k/n} \to E_{k/n} \times \text{Scale} \tag{49}$$

$$\text{– Slope :} \qquad E_{k/n} \to E_{k/n} \begin{cases} E_{k/n} \to E_{k/n} & \text{if } E_{k/n} \geq E_{k/n}^{\text{thresh.}} \\ \sigma \times \left(\frac{E_{k/n}}{E_{k/n}^{\text{thresh.}}} \right)^{\text{Slope}} & \text{otherwise} \end{cases} \tag{50}$$

The cross-section parametrisations obtained from these transformations are called normalisation, scale and slope (NSS) cross-sections. Adding nuisance parameters improves the quality of the fitting results. However, it makes the fitting procedure computationally more expensive. To reduce the required computational time only a normalisation and energy scale are used for inelastic cross-sections, while a normalisation and a slope are sufficient to account for production cross-section parametrisations [29]. For every production or destruction reaction relevant to the B/C flux ratio, NSS nuisance parameters are selected such that $\sigma^{\text{NSS}}/\sigma^{\text{ref}} \pm 1\sigma$ - obtained from a Gaussian distributed samples $(\mu, \sigma)^{\text{Norm, Scale, Slope}}$ - covers the different nuclear cross-section parametrisations. For the minimisation procedure we take NSS parameters from [29]. These can be found in Table 3.

Reaction (max. impact on B/C)	Norm.	Scale	Slope	$E_{k/n}^{\text{thresh.}}$ [GeV/n]
	$\mu - \sigma$	$\mu - \sigma$	$\mu - \sigma$	$\mu - \sigma$
$^{16}\text{O} + \text{H}$ (1%)	$1.030 - 0.04$	$0.7 - 0.5$	-	-
$^{12}\text{C} + \text{H}$ (3%)	$1.015 - 0.04$	$0.8 - 0.5$	-	-
$^{11}\text{B} + \text{H}$ (2%)	$0.980 - 0.04$	$0.7 - 0.4$	-	-
$^{16}\text{O} + \text{H} \rightarrow^{11} B$ (15%)	$0.96 - 0.18$	-	$0.00 - 0.15$	$5 - 0$
$^{16}\text{O} + \text{H} \rightarrow^{10} B$ (9%)	$0.93 - 0.10$	-	$0.00 - 0.15$	$5 - 0$
$^{12}\text{C} + \text{H} \rightarrow^{11} B$ (12%)	$1.10 - 0.12$	-	$0.03 - 0.15$	$8 - 0$
$^{12}\text{C} + \text{H} \rightarrow^{14} B$ (12%)	$1.07 - 0.15$	-	$0.00 - 0.15$	$5 - 0$

Table 3: μ and σ values for Gaussian distributed nuisance parameters for NSS parametrisation. [29]

3.1.2 Linear combination (LC)

Another way to obtain parametrisations of nuclear cross-sections to use as nuisance parameters is by taking a linear combination (LC) of the existing cross-section parametrisations [29]:

$$\sigma^{\text{LC}} = \sum_i C_i \times \sigma_i \tag{51}$$

where i runs over the available cross-section parametrisations and C_i is a coefficient that should be close to unity in order to include all existing parametrisations more or less equally. The coefficient C_i is computed as

$$\sum_i C_i = \mu_C^{\text{user}} \pm \sigma_C^{\text{user}} \tag{52}$$

where we use $(\mu_C, \sigma_C)^{\text{inel}} = (1, 0.04)$ and $(\mu_C, \sigma_C)^{\text{prod}} = (1, 0.15)$ for ineleastic and production cross-sections, respectively. This leads to a penalty term in the χ^2 called $\chi^2_{\text{LC-penalty}}$ that is described in Section 3.3. In the minimisation procedure the C_i coefficient is taken to be uniformly distributed on the interval [-0.5,1.5] and it is not allowed to take any value outside of this domain.

3.2 Generation of mock data

In this project we make use of two different models. The first model that is used in the statistical analysis is named Model A. The model includes diffusion, reacceleration and convection, and is most flexible in the low-rigidity regime of the B/C CR spectrum. Model A is the QUAINT model (see Section 2.3) and contains 5 free transport parameters: V_A, V_c, η_t, K_0 and δ. The high-rigidity parameters R_h, δ_h and s_h are treated as nuisance parameters.

The second model that is used in this project is named Model B. The model only includes diffusion and is most flexible in the low-rigidity regime of the B/C CR spectrum. The low-rigidity smoothness break parameter s_l has minor impact on fitting results and is therefore fixed at $s_l = 0.04$ [29]. Model B is the SLIM model (see Section 2.3) and contains 4 free parameters: K_0, δ, R_l and δ_l. The high-rigidity parameters R_h, δ_h and s_h are treated as nuisance parameters.

In order to investigate the transport parameter behavior within AMS-02-like data, we generate mock data that is similar to the original AMS-02 data within its uncertainty range. This is done in the following way. First, the model describing CR transport is selected. In this project

model A and model B are used. With this model a *reference flux* or *mock flux* comparable to AMS-02 data is generated by fixing the transport parameters and drawing a B/C flux ratio with the use of the USINE software.

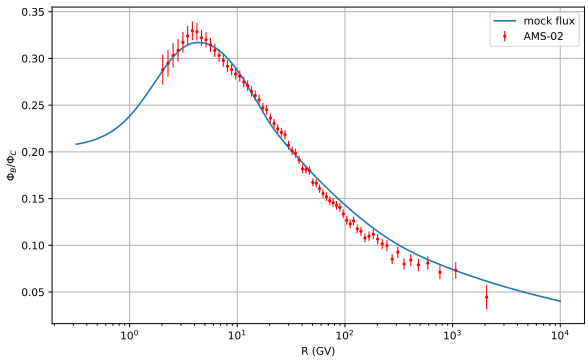

Figure 24: B/C mock flux (generated with USINE software) and AMS-02 data.

Figure 24 shows the generated mock flux together with AMS-02 data. The mock flux does not have to match the real AMS-02 data perfectly, as we are only interested in the behavior of the transport parameters. For the purpose of this work, a qualitative agreement is sufficient. Mock data points are obtained by taking B/C mock flux values at AMS-02 data rigidities and subsequently adding AMS-02 B/C statistical uncertainties. This is done by applying white Gaussian noise to the AMS-02 B/C statistical uncertainties normalised by AMS-02 B/C data. Mock data points are thus computed as

$$y_k^{\text{mock}} = y_k^{\text{model}} \times \left(1 + \mathcal{G}(0,1)\frac{\sigma_k^{\text{data}}}{y_k^{\text{data}}}\right) \tag{53}$$

With this a single set of mock data is generated. An example of such a mock data set is displayed in Figure 25. In this figure "mock flux" denotes the mock flux generated by USINE and "mock data" denotes the AMS-02-like data set generated at AMS-02 rigidities and based on AMS-02 uncertainties.

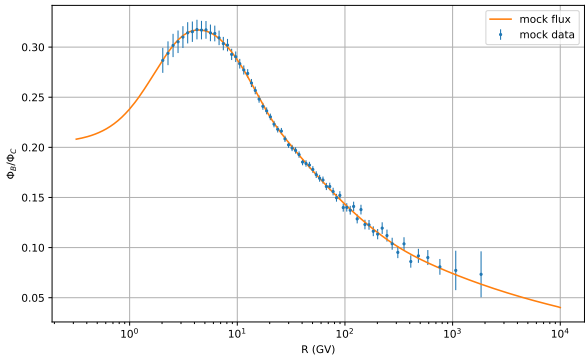

Figure 25: B/C mock flux (generated with USINE software) and AMS-02-like mock data.

The transport parameter space can then be investigated by generating many realisations of mock data sets and subsequently finding the best fit transport parameters.

The employed procedure can be summarised as follows:

1. Generate B/C mock flux similar to the real AMS-02 B/C flux ratio.
2. Draw B/C flux ratio values from the mock flux at AMS-02 data rigidities and add noise based on AMS-02 statistical uncertainties to this.
3. Repeat this procedure many times to obtain many mock data sets to get a statistically sound determination of the cosmic-ray propagation parameters.

3.3 Fitting the mock data

For every data set the transport parameters are fitted with the MINUIT package [40] in USINE [33]. For every minimisation procedure performed by USINE a χ^2 analysis implemented in the software is returned along with the obtained best fit parameters. The generic form of the χ^2 used for the analysis of CR data with USINE is

$$\chi^2 = \sum_t \left[\sum_q \left(\mathcal{D}_{\rm cov}^{t,q} + \mathcal{N}^{t,q} \right) + \mathcal{N}^t \right] + \mathcal{N} \tag{54}$$

in which we account for various modulation levels by summing over all time periods t, meaning that we take into account the solar modulation that depends on the time at which the observations were carried out. We also sum over all quantities q, i.e. cosmic-ray species, that are selected in the minimisation. The quantities $\mathcal{D}_{\rm cov}$ and $\mathcal{N}$ denote the covariance and nuisance, respectively. Both are described below.

The distance between the data and model is measured by the quadratic distance $\mathcal{D}_{\rm cov}$. This is described with the use of a covariance matrix $\mathcal{C}$ as

$$\mathcal{D}_{\rm cov} = \sum_{i,j=1}^{n_E,n_E} ({\rm data}_i - {\rm model}_i)(\mathcal{C}^{-1})_{ij}({\rm data}_j - {\rm model}_j) \tag{55}$$

and correlates energy bins i and j of which there are n_E in total. If no correlations are present, the covariance matrix $\mathcal{C}$ is a diagonal matrix and equation 55 reduces to

$$\mathcal{D}_{\text{no-cov}} = \sum_{k=1}^{n_E} \frac{({\rm data}_k - {\rm model}_k)^2}{\sigma_k^2} \tag{56}$$

where σ_k is the systematic error on data point k.

One can also build a covariance matrix of relative errors $\mathcal{C}_{\rm rel}^{\alpha}$, where α denotes the type of systematic AMS-02 uncertainty, e.g. statistical, acceptance, scale or unfolding. This covariance matrix of relative errors can then be related to the covariance $\mathcal{C}^{\alpha}$ through either the data or model, i.e.

$$(\mathcal{C}_{\rm model}^{\alpha})_{ij} = (\mathcal{C}_{\rm rel}^{\alpha})_{ij} \times {\rm model}_i \times {\rm model}_j \tag{57}$$

$$(\mathcal{C}_{\rm data}^{\alpha})_{ij} = (\mathcal{C}_{\rm rel}^{\alpha})_{ij} \times {\rm data}_i \times {\rm data}_j \tag{58}$$

Different types of nuisance parameters appear in models:

1. $\mathcal{N}$: global nuisance parameters. They are related to the model and unrelated to the data, for example CR cross-sections.

2. $\mathcal{N}^t$: time-dependent nuisance parameters. For example the solar modulation parameter Φ that varies over time.

3. $\mathcal{N}^{t,q}$: data-dependent nuisance parameters. An example of these are systematic errors on data. They can be used as an alternative to the use of a covariance matrix.

In general, nuisance parameters can be included in analysis with any probability distribution depending on knowledge about the physical process or prior experiments, for example. However, USINE enables the use of nuisance parameters through Gaussian distributions. As a consequence, every nuisance parameter contributes

$$\chi^2 = \frac{(y - \bar{y})^2}{\sigma_y^2} \tag{59}$$

to the χ^2 of equation 54. Here, y, $\bar{y}$ and σ_y^2 represent the tested value, mean value and variance of the parameter, respectively.

Moreover, from the extra constraint posed on the LC parametrisation as written in equation 52 we obtain an additional penalty contribution to the χ^2 that is given by

$$\chi^2_{\text{LC-penalty}} = \left(\frac{\mu_C - \sum_i C_i}{\sigma_C} \right)^2 \tag{60}$$

3.4 Mock data fit configurations

The mock data sets are fitted using different settings. Below we describe the various configurations used in the analysis.

- *Propagation parameters* (2): Two different models are considered, model A and model B as described in Section 2.3. We recall that model A is a diffusion-convection-reacceleration model and we use K_0, δ, η_t, V_a and V_c as free parameters. Model B is a pure diffusion model. Here we use K_0, δ, R_l and δ_l as free parameters.
- *Cross-section parametrisations* (2): Two different ways of cross-section parametrisation described in Section 3.1 are considered: the Normalisation, Scale and Slope (NSS) parametrisation and the Linear Combination (LC).
- *Cross-section types* (4): Four ways of including cross-sections as nuisance parameters in the analysis are considered.
  - *No nuis*: does not include cross-sections as nuisance parameters. Instead it only uses free propagation parameters.
  - *Inel*: Inelastic cross-sections are included in the analysis as nuisance parameters.
  - *Prod*: Production cross-sections are included in the analysis as nuisance parameters.
  - *Inel + Prod* Both inelastic and production cross-sections are included in the analysis as nuisance parameters.

This means that for n mock data sets, we conduct $n \times 2 \times 2 \times 4 = 16n$ minimisation procedures.

3.5 Results

Below we describe the results of the analysis of the AMS-02-like data. Table 4 shows the values of the model parameters used in the analysis. The free parameters of the models are indicated with an asterisc, and they are used in the generation of the mock data. Therefore, they are considered the true parameter values in the following analysis. Our analysis will be performed in two independent scenarios, called unbiased and biased. In the biased case we generate and fit the mock data using the same choice of cross-section parametrisation. In the biased case we generate the mock data with a given parametrisation and with fit using a different one. The results for the two options will be shown in the following.

Parameters	model A	model B
Low-rigidity parameters		
V_A [$\mathrm{km\,s^{-1}}$]	85*	-
V_c [$\mathrm{km\,s^{-1}}$]	10*	-
η_t	-0.8*	-
R_l [GV]	0.14	4.5*
δ_l	-	0.5*
s_l	-	0.04
Intermediate-rigidity parameters		
$\log_{10} K_0$ [$\mathrm{kpc^2\,Myr^{-1}}$]	-1.23*	-1.18*
δ	0.45*	0.45*
High-rigidity break parameters		
R_h [GV]	310	200
δ_h	0.14	0.14
s_h	0.04	0.04
Additional parameter settings		
α	2.3	2.3
Φ [GV]	0.73	0.73
L [kpc]	8	8
h [kpc]	0.1	0.1

Table 4: Parameter settings of model A and B for generation of mock data. Free parameters are denoted with * and the corresponding values displayed are used for generating a mock flux and are called "true values" in the analysis. These values are chosen such that the resulting B/C flux ratio provides a qualitative description to the B/C flux ratio measured by AMS-02.

Figure 26 shows the result of the analysis of 1000 mock data sets for the two models. The best fit parameter values that are obtained in the analysis are displayed as contour plots where the lines indicate the 1σ uncertainties of the probability distributions of the transport parameters. Each line shows the results obtained for one of the configurations used. The crosses "+" indicate the true values, i.e. the values with which the mock flux is generated.
As expected for the unbiased case (mock data generated and subsequently fitted with the same nuclear cross-section parametrisations), the 1σ uncertainty contours obtained from the 2D probability distributions surround the true values of the transport parameters. In other words, the transport parameter values that are used to generate the mock data can be retrieved again by the fitting procedure. We also see that the configuration in which no cross-section nuisance parameters are used (black solid lines), return the smallest uncertainties and the most regular and symmetric line shapes. This shows that adding nuclear cross-sections as nuisance parameters

allows for more freedom for the transport parameters.
In both models a strong correlation between $\log_{10} K_0$ and δ is obtained. In model A we also see that V_c correlates with $\log_{10} K_0$ and δ. For example, a larger value for δ that is indicating towards Kraichnan turbulence ($\delta = 1/2$) can be accounted for by a larger convectional wind and a small diffusion coefficient normalisation K_0. The model is degenerate and allows for multiple descriptions of conditions in the Galaxy.
Another noticeable feature of Figure 26 is the different deformations of the contours for the various configurations. For example, if we look at the contours for R_l and $\log_{10} K_0$ in model B, we notice that the shapes of the blue (inelastic) and orange (production) lines are distinctly different. This can be explained by the different impact that the inelastic cross-sections have on the B/C ratio compared to the production cross-sections. If we look at the green (inelastic + production) contours, we see that these surround both the blue and orange contours. However, there still remains a difference in shape for NSS and LC contours, which confirms that the choice of model as well of the choice of cross-sections and type of cross-section parametrisations impact the results of the B/C ratio minimisation. The unbiased case can be interpreted as a sanity check. It confirms that adding cross-section uncertainties has only a marginal effect in a scenario where cross-sections are perfectly known.

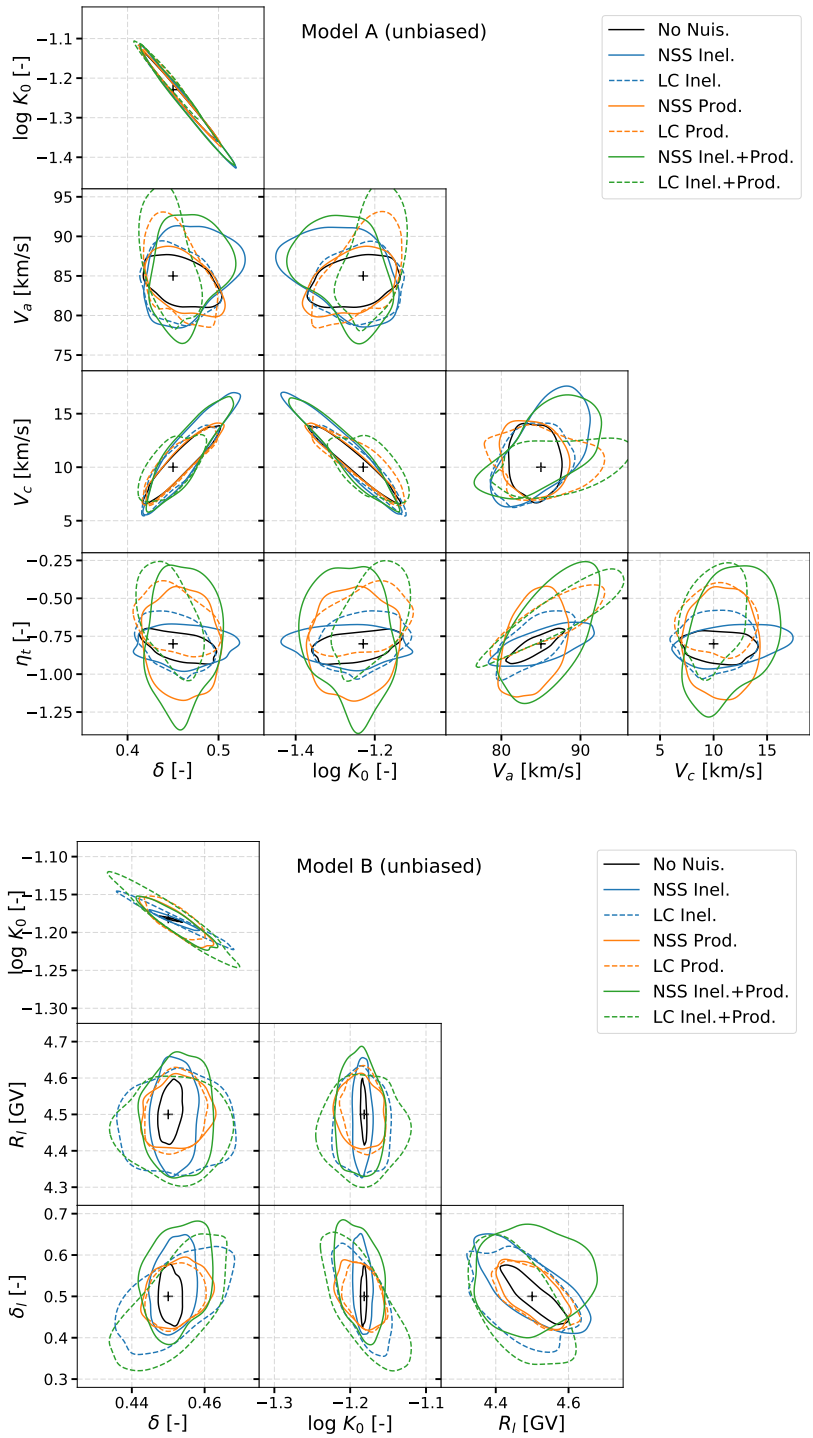

Figure 26: Two-dimensional probability distributions of the best fit transport parameter values resulting from the analysis of 1000 mock data. The contours indicate the 1σ uncertainty levels for various cross section nuisance parameter configurations. The + symbol indicates the true values of the transport parameters, i.e. the values of the transport parameters with which the mock data are generated.

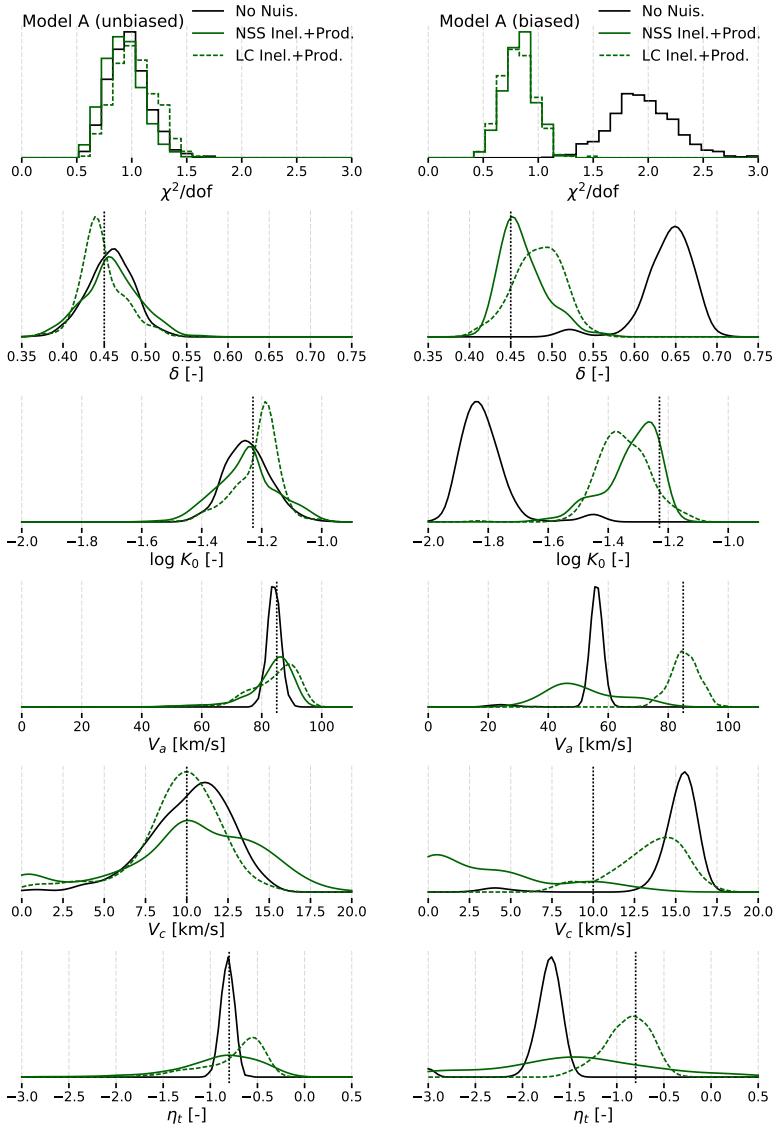

(a) (b)

Figure 27: Probability distributions of χ^2/dof and best fit transport parameters of model A obtained from the analysis of 1000 mock data for the (a) unbiased and (b) biased cases.

Figures 27 and 28 show the probability distributions of the χ^2/dof (goodness of fit) and best fit values of the free propagation parameters of models A and B, respectively. The probability distributions are obtained from the analysis of 1000 mock data. The black curve shows the configuration without cross-section nuisance parameters. The green solid and dashed curves display the configurations with inelastic and production cross-sections parametrised by the NSS and LC methods, respectively. Vertical dashed lines indicate the true values of the transport parameters, i.e. the values of the transport parameters with which the mock data is generated. The probability distributions are displayed for the biased (a) and unbiased (b) cases.
We observe that for both model A and B the minimisation procedure finds back the propagation parameters for all shown configurations in the unbiased case. This leads to a χ^2/dof (goodness of fit) probability distribution that peaks at approximately 1. For the biased case, this is not the

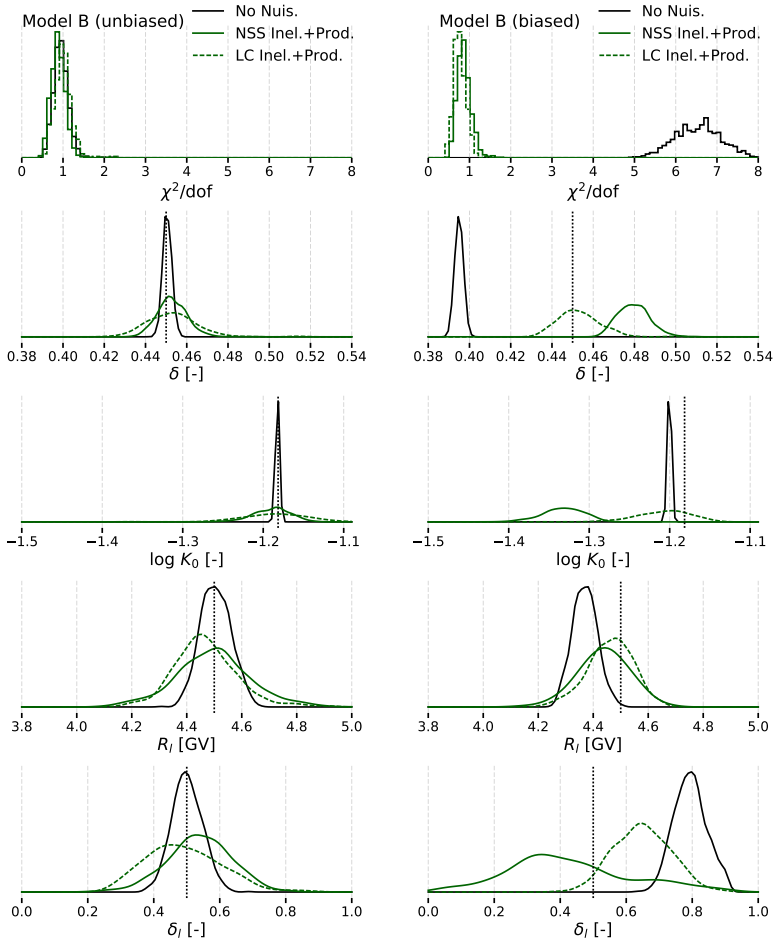

(a) (b)

Figure 28: Probability distributions of χ^2/dof and best fit transport parameters of model B obtained from the analysis of 1000 mock data for the (a) unbiased and (b) biased cases.

case. Where the configuration without cross-section nuisance parameters is not able to retrieve the true values of the transport parameters, the configurations with inelastic and production cross-sections parametrised with the NSS and LC methods do find back the true values more often. The parameter distributions are broadened and shifted towards their true values. This is also reflected in the χ^2/dof probability distribution of model A. The no nuisance parameters configuration shows a broad distribution centered around 2, while the NSS and LC configuration distributions coincide and mainly contain values below 1. This difference is even more distinct for model B, where the broad no nuisance configuration distribution peaks between 6 and 7, while the NSS and LC configuration distributions again coincide and mainly contain values below 1. We also note that the LC configuration does a slightly better job than the NSS configuration. This can be explained by the fact that with a linear combination of cross-section parametrisations of which one is used to generate the data, one can reach the true values of the cross-sections. With the NSS method, the true cross-sections can only be approached. The better performance of the LC parametrisation method becomes clear especially for the $\log_{10} K_0$ and δ distributions of model B. If the best fit value distribution of one of these strongly correlated transport parameters

is shifted, this causes the distribution of the other parameter to be shifted away from its true value too.
To conclude Figure 28, we find that assuming wrong nuclear cross-sections can strongly bias the model fit, generating a bias on the transport parameters.

In order to see how well the true values of the nuisance parameters are retrieved in the minimisation procedure, we present Figure 29. In this figure we show the probability density of best fit cross-section nuisance parameters obtained from the analysis of 1000 mock data. The figure shows the results for the inelastic *and* production NSS and LC configurations, each with unbiased and biased analysis of model A and B. The nuisance parameters for various channels are shown and the impact that the channels have on the B/C ratio is indicated in brackets after the channel. For the NSS analysis normalised and centered parameters are shown. For the LC analysis the coefficients C_i are shown between zero and one. The crosses and horizontal thick black lines indicate the median values and 1σ uncertainties, respectively. On the y-axis the probability density of the obtained cross-section nuisance parameter values are displayed in color: red for unbiased and blue for biased analysis.
For the NSS analysis, we expect the unbiased nuisance parameters to be centered at zero, since in this case we find back the same cross-sections as the ones with which the mock data was generated. This is indeed what we observe. However, the biased nuisance parameters indicate that the true values of the cross-sections are not always found back. Deviations up to 1.5σ occur, which means that the NSS parametrisation method does not always find the correct cross-sections when starting from a different set of nuclear cross-section parametrisations.
For the LC analysis, the mock data are generated with T99 [41, 42] inelastic and W03 [43] production cross-sections. Therefore, for the unbiased analysis (red in Figure 29), we expect the coefficients $C_{W03} \approx 1$ and $C_{T99} \approx 1$. The mock data are not generated with W96 [44] inelastic and G17 [45, 46] production cross-sections. Therefore, for the unbiased analysis we expect the coefficients $C_{G17} \approx 0$ and $C_{W96} \approx 0$. Analogously, for the biased analysis (blue in Figure 29), we expect the coefficients $C_{W03} \approx 0$, $C_{T99} \approx 0$, $C_{G17} \approx 1$ and $C_{W96} \approx 1$, since the mock data of the biased analysis is generated with the use of W96 inelastic and G17 production cross-sections. We see that the expectations described are what we observe in the analysis. The inelastic channels show the broadest distributions. However, these have minor impact on the B/C ratio (up to 3%).

From Figure 29 we can see that the LC parametrisation method performs slightly better than the NSS method. However, we should note that this can be due to the fact that the true cross-sections with which the mock data are generated are included in the LC. There is no guarantee that this method will work as well as it does in this analysis when a set of unknown nuclear cross-section parametrisations is used, or in fact, real world data. Therefore we cannot conclude which method performs best and both methods should be included in the analysis of real CR observational data.

However, we should note that concerning the impact of cross-section uncertainties and which reaction channels are to be used as nuisance parameters, the conclusions are highly dependent on the choice of data uncertainties. In this work we have used only statistical uncertainties from real AMS-02 data to separate cross-section uncertainties from other data uncertainties. This leads to a scenario that is too conventional and making use of other uncertainties would lead to a smaller influence of cross-section uncertainties on the determination of transport parameters, as more freedom is provided by other more dominant uncertainties, such as systematics [8, 9]. Showing that the conventional scenario works, justifies our approach for handling cross-section uncertainties.

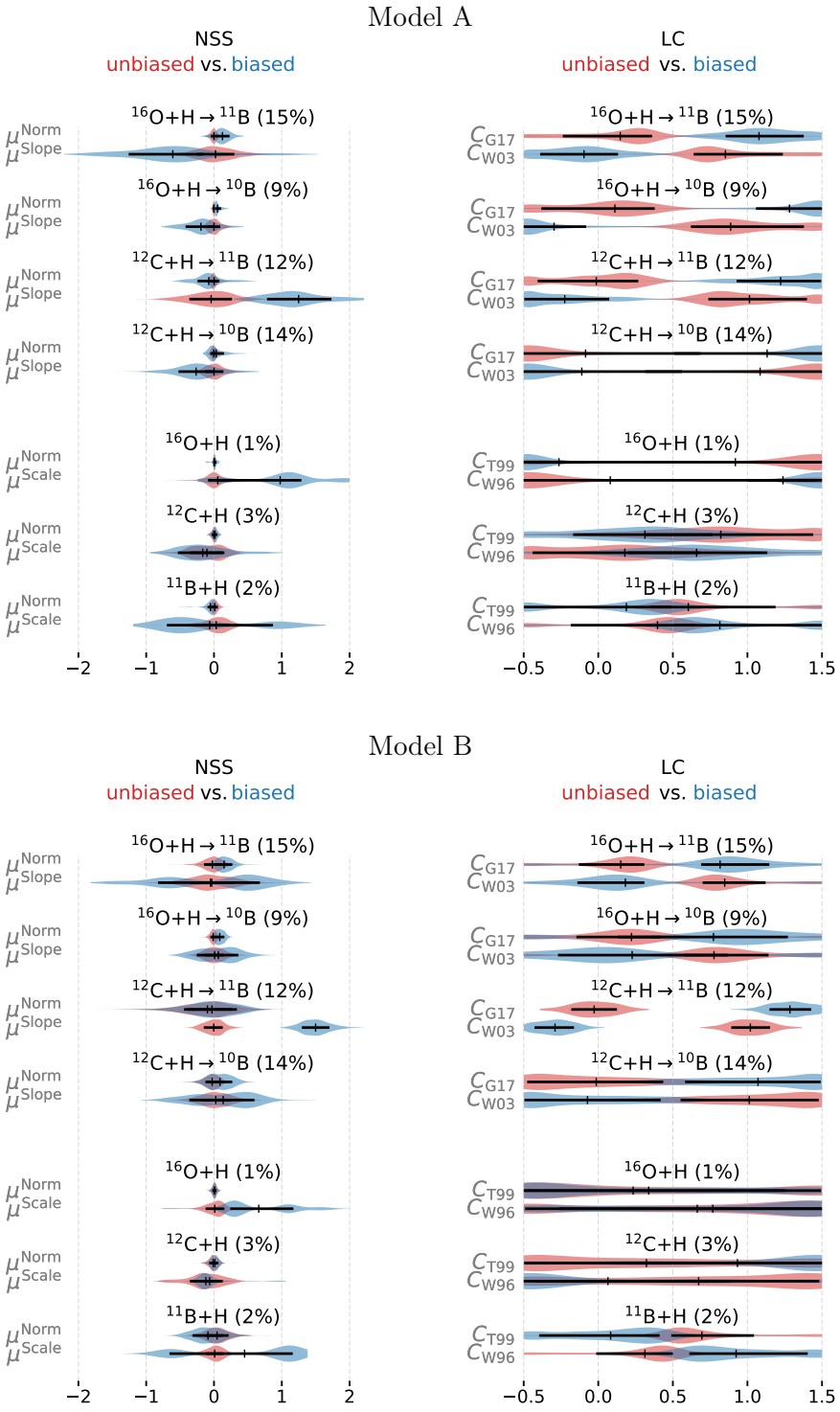

Figure 29: NSS and LC cross section parametrisation nuisance parameters from the unbiased and biased analysis of 1000 mock data for model A and B of various prodution and destruction channels. For the NSS analysis normalised and centered parameters are shown. For the LC analysis the coefficients C_i are shown between zero and one. The + symbols and horizontal thick black lines indicate the median values and 1σ uncertainties, respectively. On the y-axis the probability density of the obtained cross section nuisance parameter values are displayed in color, red for unbiased and blue for biased analysis.

4 Constraints on the cosmic-ray propagation from light nuclei

The B/C flux ratio is widely used to study the propagation of galactic cosmic rays, i.e. in the GeV to TeV energy range. However, given the wealth of precise CR data made available in the past decades by the current generation experiments, we are for the first time able to extend the study of CR propagation in the galaxy using additional measurements that can potentially expand our knowledge on the topic. In particular, the study of light CR nuclei, such as protons, deuterons, and helium (composed of two stable isotopes, ^{3}He and ^{4}He), can help probe a different Z/A regime and thus the universality of propagation. CR deuterons are the most abundant CR secondary species, accounting for about 2% of protons. The current most precise measurements of CR deuterons are provided by the PAMELA experiment [47] and extend up to 1 GeV/n. In this chapter, we will take advantage of the deuteron flux and the ^{2}H/^{4}He flux ratio to test the CR propagation with the USINE software, and we will compare our results with the B/C results from the literature.
Deuterium is considered to be mainly a secondary CR species, because it is not an end product of fusion processes in stars. Interactions with the ISM are important in the production of deuterium. In particular the spallation of ^{3}He and ^{4}He is the main deuterium production process [48]. Another important process for the production of deuterium is the $p + p \rightarrow \pi + d$ interaction. Figure 30 displays the fractional contribution of parent species to the production of deuterium.

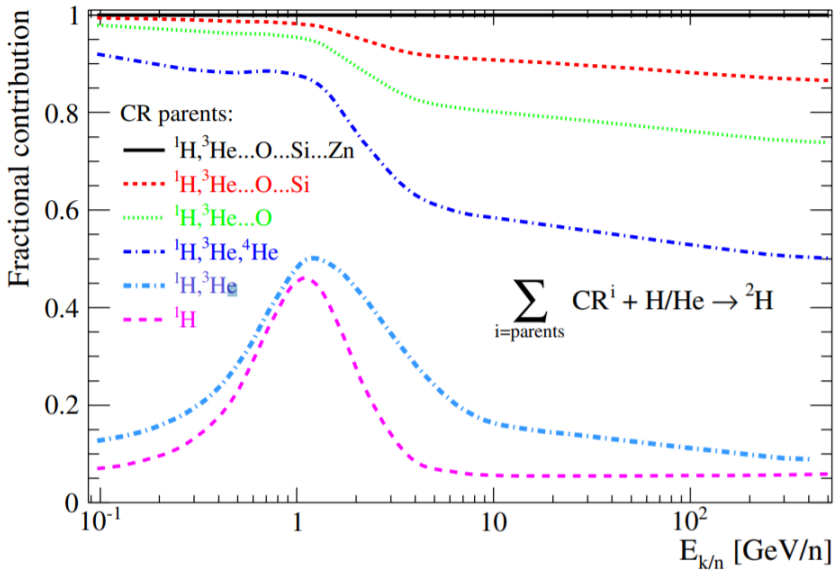

Figure 30: Fractional contribution to the deuterium flux from parent species, as a function of kinetic energy per nucleon [49].

The fractional contribution of ^{1}H, ^{3}He and ^{4}He makes the deuterium-to-helium and deuterium-to-hydrogen flux ratios important quantities to set constraints on the CR propagation models. However, these flux ratios are increasingly more difficult to measure for higher energies, particularly above 0.1 GeV/n, because detectors must have a high mass resolution in order to distinguish deuterium from protons. Figure 31 displays the ^{2}H/H flux ratio measurements from various experiments. In this work, we chose to take into account only the results from the PAMELA experiment, because they are the most recent and the most precise.
For completeness, it is worth mention that the SOKOL experiment has measured one data point of the the ^{2}H/He flux ratio at the TeV.

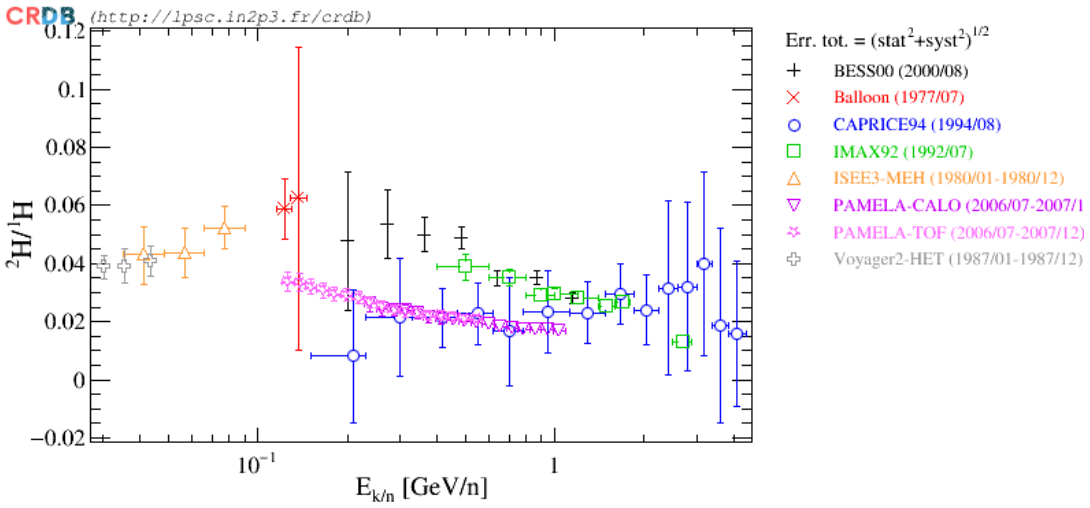

Figure 31: Measurements of the deuterium-to-hydrogen flux ratio from different experiments, as a function of kinetic energy per nucleon. [50]

4.1 Theoretical prediction for the deuteron flux

In the following we will perform preliminary studies on the deuterium flux with the use of the USINE code. We will investigate the influence on the deuterium flux of the choice of the propagation model, effects of individual physical processes and variation of the half-height of the diffusive halo and of the solar modulation potential.

We take the SLIM model as a reference. CR species from ^{1}H up to ^{60}Fe are simulated in order to include all the possible channels through which deuterium can be formed. The half-height of the diffusive halo L is set to 5 kpc and a solar modulation potential $\Phi = 0.7$ GV is used. These values are chosen from the research on galactic halo size in the light of recent AMS-02 data conducted by [36] and the solar modulation levels found in the studies of secondary to primary species by [29, 38].

In the following we will present preliminary studies of the deuterium flux. We consider the three benchmark models BIG, SLIM and QUAINT, shown in Figure 32. We obtain very similar deuterium flux spectra for the most generic BIG model and its limiting case model SLIM. These spectra are essentially the same up to a few percent. For the QUAINT model however, we observe relative differences $\sim 9\%$ and $\sim 13\%$ around $R \approx 2$ and 4 GV, respectively. The discarding of the low energy break in the diffusion coefficient (QUAINT) appears to have a significant influence on the deuterium flux.
Moreover, we inspect the effect of individual physical processes such as convective winds, reacceleration, coulomb losses and destruction, on the deuterium flux. We start from a configuration that only includes the production of primary and secondary cosmic rays, while no convective winds, reacceleration, coulomb losses and destruction are taken into account. We progressively add these processes one by one. Figure 33 displays the results of this pedagogic exercise, where the initial configuration is shown in cyan. We find that the largest flux is obtained by the configuration that only includes the production of primary and secondary cosmic rays. Then we see that the processes that affect and reduce the deuterium flux, in order of least to most important, are reacceleration, Coulomb losses and destruction. What stands out most is that the

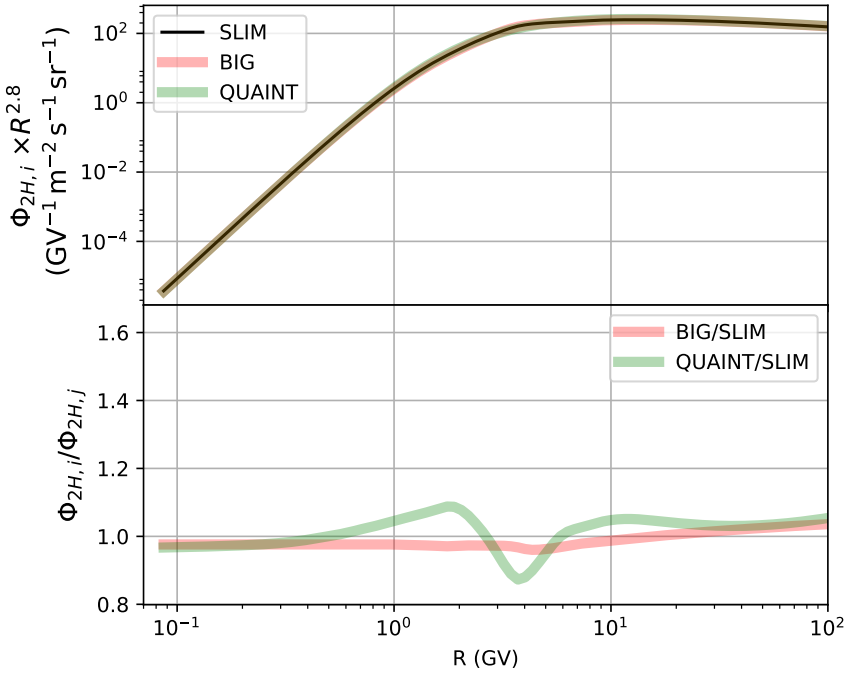

Figure 32: Comparison of the three benchmark models BIG, SLIM and QUAINT for the ^{2}H flux. The top panel shows the flux generated by USINE for different configurations, while the bottom panel shows the ratio of one of the configurations compared to the SLIM configuration to obtain the relative differences between the configurations.

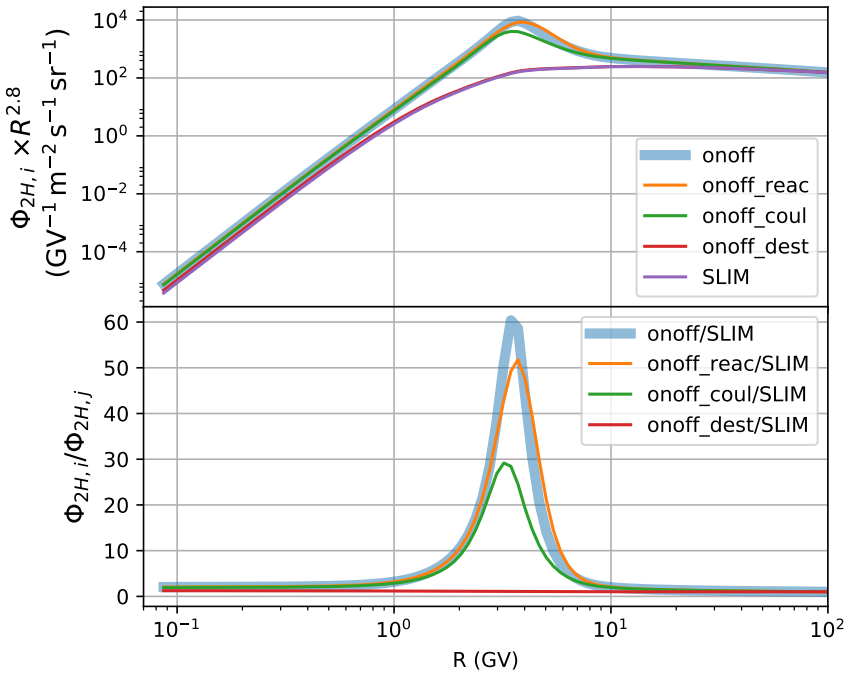

Figure 33: Comparison of the impact of various physical processes on the ^{2}H flux. We refer to the text for clarification of the different configurations. The top panel shows the flux generated by USINE for different configurations, while the bottom panel shows the ratio of one of the configurations compared to the SLIM configuration, in order to compare the configurations.

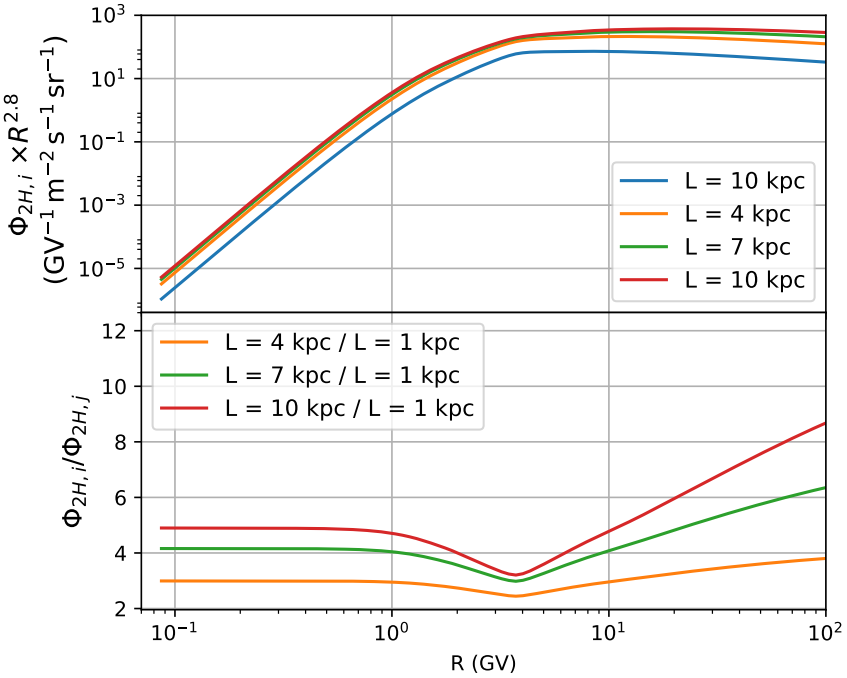

Figure 34: Comparison of the impact of various values of L (the half-height of the diffusive halo) on the ^{2}H flux. The top panel shows the flux generated by USINE for different configurations, while the bottom panel shows the ratio of one of the configurations compared to the configuration with $L = 1$ kpc to obtain the relative differences between the configurations.

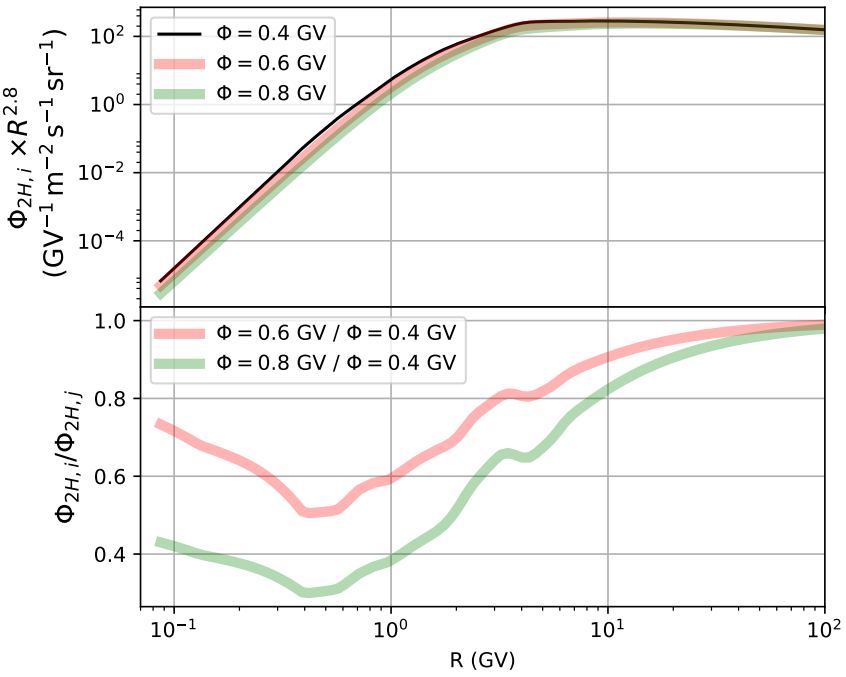

Figure 35: Comparison of the impact of various values of the solar modulation on the ^{2}H flux. The top panel shows the flux generated by USINE for different configurations, while the bottom panel shows the ratio of one of the configurations compared to the configuration with $\Phi = 0.4$ GV to obtain the relative differences between the configurations.

destruction process has by far the most impact on the deuterium flux, reducing it by a factor of

60 compared to the simulation that only includes primary and secondary species. In fact it has such a large impact that it shows a one-to-one behaviour with the basis SLIM configuration that includes much more relevant processes, meaning that this process on itself is responsible for the final deuterium flux and other processes are of minor importance.

Figure 34 shows the comparison of the impact of various values of L (the half-height of the diffusive halo) on the deuterium flux. We see that the value of size of this parameter impacts the flux significantly. If we compare the extreme cases in which $L = 1$ and $L = 10$ kpc are used, the relative difference ranges from a factor 3 at 4 GV up to a factor 8 at 70 GV.
Lastly we reflect on the impact of the solar modulation on the deuterium flux. Figure 35 shows the comparison of the impact of various values of the solar modulation on the deuterium flux. We observe that the deuterium flux is strongly affected by the value of the solar modulation potential, which is expected as for any other CR species, especially up to tens of GV. Comparison of the fluxes from simulations with $\Phi = 0.4$ GV and $\Phi = 0.8$ GV shows a large relative difference at low rigidities, up to a factor 3 at $R \sim 0.45$ GV. The relative difference gradually reduces as the rigidity increases. As expected, the value of the solar modulation potential does not affect flux at high rigidities, particularly above 7 GV.

4.2 Fitting the ^{2}H flux and ^{2}H/^{4}He flux ratio

We have computed the deuteron flux using the transport parameters available in the literature [38] and obtained from the fit to B/C from AMS-02. Figure 36 shows our model, together with the AMS-01 [51] and PAMELA data [47], from 0.1 to 1 GeV/n. In this simulation, we used a solar modulation potential $\Phi = 527.8$ MV, consistent with the solar modulation for the period of data taking of the PAMELA experiment. The simulations are underestimating the deuterium flux over the whole energy range by approximately a factor of two.

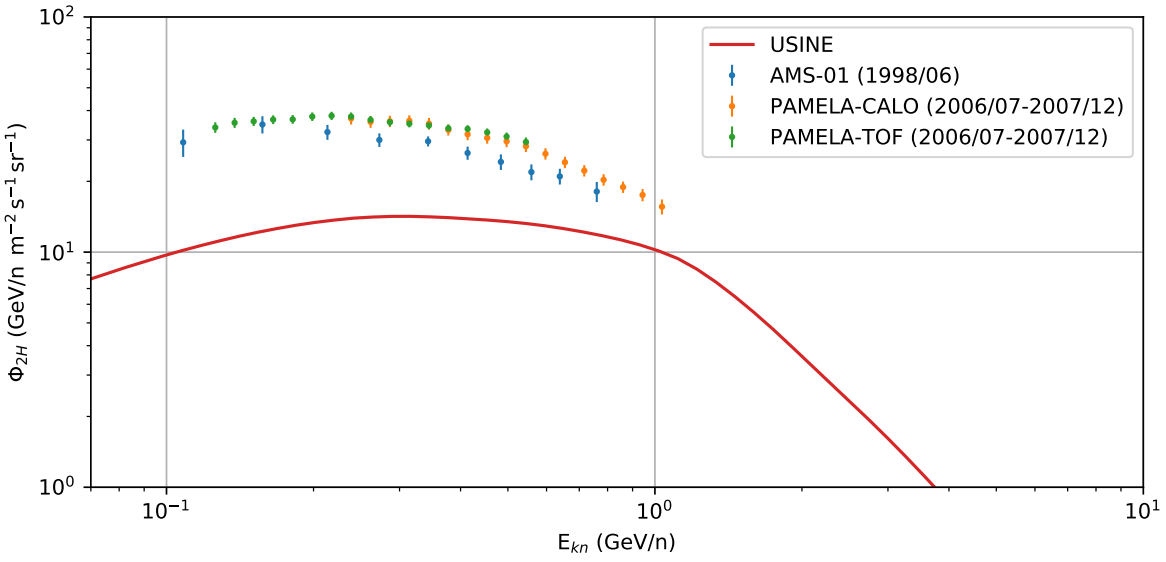

Figure 36: Deuterium flux computed by USINE with the SLIM model and the B/C best fit parameters from [38] together with deuterium measurements from PAMELA [47] and AMS-01 [51].

To obtain the best fit transport parameters for deuterium data, we apply the USINE minimisation procedure to the ^{2}H flux and ^{2}H/^{4}He flux ratio from PAMELA [47] measurements with the use of the benchmark models BIG, SLIM and QUAINT. For the BIG model we fix $\eta_t = 1$, because the effect of the non-relativistic parameter is degenerated with that of δ_l. The minimisations for these benchmark models return χ^2_{min}/dof values on a range 0.15 - 0.39. This indicates a decent fit, since we do not make use of cross-section nuisance parameters and the PAMELA measurements provide a small amount of data points on a limited energy range. The χ^2_{min}/dof is has a smaller value for all three models, compared to the B/C flux ratio fitted by [35], who make use of one cross-section nuisance parameter and obtain χ^2_{min}/dof$\sim$ 1 for all three benchmark models. The χ^2_{min}/dof can be reduced significantly to values close to zero by the use of cross-section nuisance parameters, as [38] shows. The results of the the ^{2}H flux and ^{2}H/^{4}He flux ratio fits are presented in Figure 37 together with the B/C best fit values from [38].

The first panel shows the fit value obtained for δ, nameely the spectral index of the high-ridigity diffusion coefficient. The result for δ obtained from the fit to the ^{2}H flux and ^{2}H/^{4}He flux ratio have significant uncertainties with respect to the δ value obtained from the B/C analysis. This large uncertainty is caused by the fact that while the measurements of the PAMELA ^{2}H flux and ^{2}H/^{4}He flux ratio are limited to 1 GeV/n, the B/C is measured by AMS-02 up to the TeV, and given that δ is a parameter that describes the high-rigidity diffusion, the limited range of the PAMELA data gives less predictive power on δ. We observe the same effect for the three propagation scenarios, i.e., BIG, SLIM, and QUAINT.
The fit results for the normalisation factor of the diffusion coefficient K_0, displayed in the second panel, differ for the three propagation scenarios. For the SLIM model, the values of K_0 obtained from the fit to three quantities are consistent within the uncertainties. For QUAINT, the K_0 result obtained from B/C is in tension with the result of ^{2}H. Still, these results are consistent with the result obtained from the ^{2}H/^{4}He flux ratio, given its more considerable uncertainty. For BIG, we also observe a tension with B/C results.
Looking at the low-rigidity parameters, especially R_l and δ_l, our results for the SLIM model obtained from the fit to the light species agree with those of the B/C. We observe a mild tension with the B/C results for the BIG model, partly mitigated by the significant uncertainties obtained from the fit to the ^{2}H flux. The results for V_a and V_c are also mildly in tension with the results from the B/C. However, this is often recovered by significant uncertainties.

Based on these results, and also because the diffusion is not the most relevant physical process that affects the propagation in the energy range of interest for the PAMELA data, we decided to perform another test and fix the δ and K_0 values to the B/C values, thus decreasing the number of fit parameters. These results are shown in Figure 38 and the minimisations return a χ^2_{min}/dof on a range 0.21 - 0.48, again indicating decent fits.
Our result for R_l is in tension with the result from the B/C, for both SLIM and BIG, while this parameter is not used for QUAINT. However, the tension is at times mitigated by the significant uncertainties on the parameter values from the fit to ^{2}H flux or ^{2}H/^{4}He flux ratio. A similar result is found for the δ_l. While the results for R_l obtained from the B/C are more significant than those obtained from the fit to the light species, we observe the opposite effect for δ_l: this is probably because these parameters are largely correlated.
Our results for V_a and V_c are also mildly in tension with the results from the B/C. However, this tension is often recovered by significant uncertainties. Finally, our results for the QUAINT model hint at the presence of reacceleration (V_a around 50 km/s) and the absence of convection, in agreement with the B/C results. Tension with the B/C results is also found for the very low

energy parameter η_t that is only used in the QUAINT model.

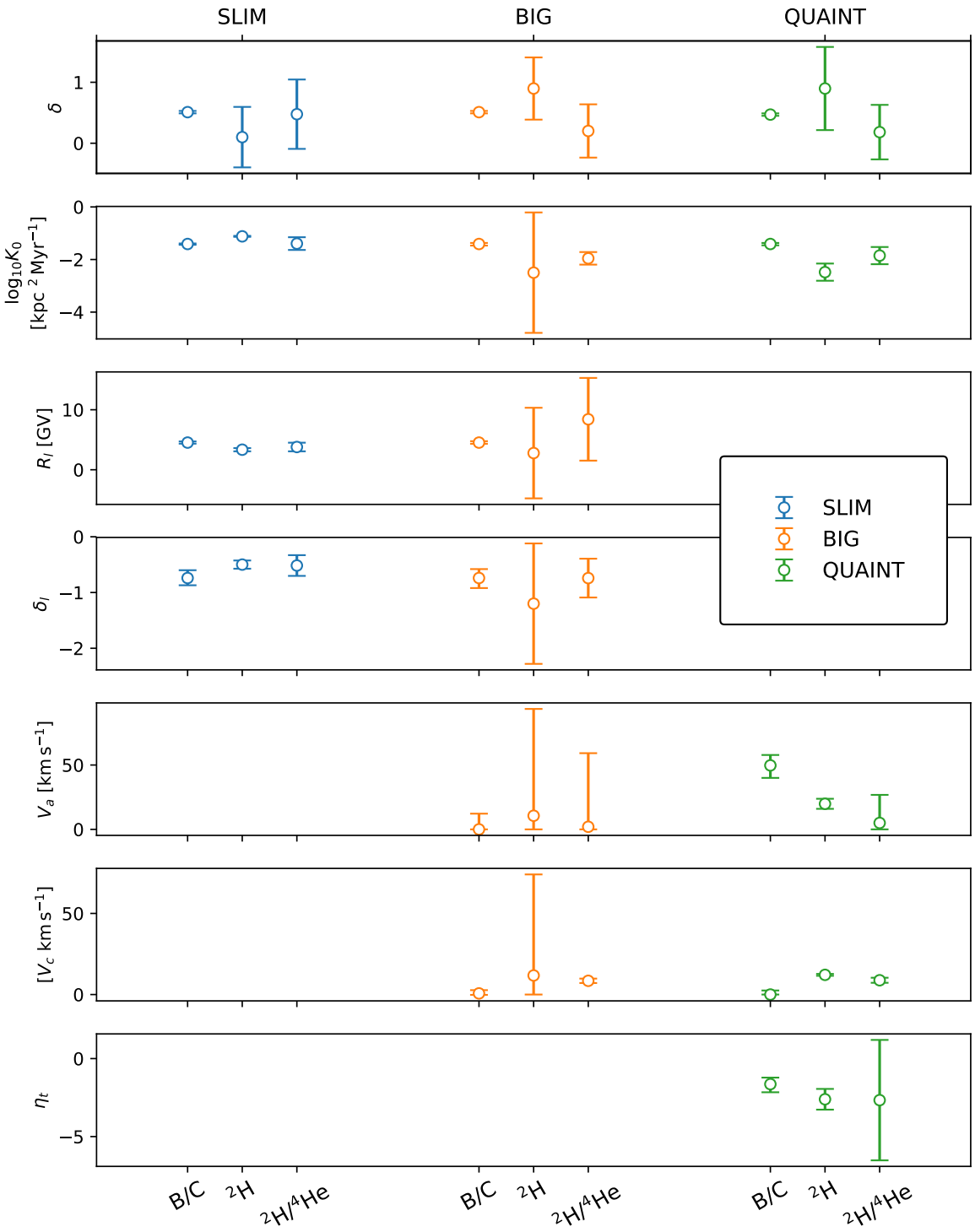

Figure 37: Best fit parameter values resulting from the minimisation of the B/C flux ratio [38], deuterium flux and ^{2}H/^{4}He flux ratio.

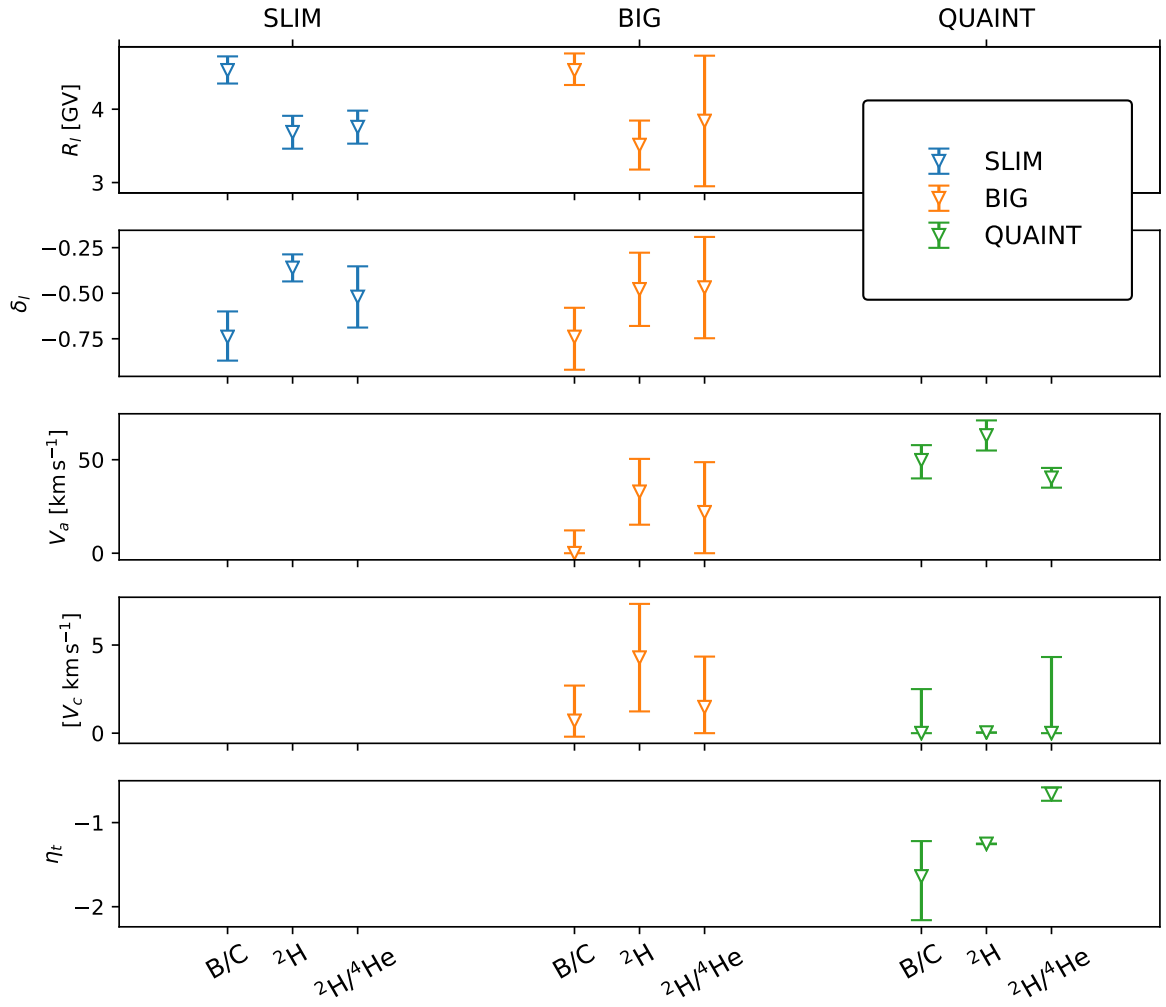

Figure 38: Best fit parameter values resulting from the minimisation of the B/C flux ratio [38], deuterium flux and ^{2}H/^{4}He flux ratio. Parameters δ and $\log_{10} K_0$ are fixed.

To conclude, fitting the deuteron flux and the ^{2}H/^{4}He flux ratio measured by PAMELA to our model, we are not able to provide a significant improvement on the understanding of the propagation with respect to the results obtained from the B/C flux ratio measured by AMS-02 up to the TeV. A better modelisation of the cross-sections and the use of nuisance parameters in the fit could improve our result, but this is beyond the scope of this work. The precise measurement of the deuteron flux from the AMS-02 experiment, extending for the first time up to 10 GeV/n, will undoubtedly provide better constraints on the propagation parameters.

5 Conclusions

The unprecedented percent precision measurements of the current generation space-based experiments, particularly the PAMELA and the AMS-02 detector, have revealed unexpected features in galactic CR fluxes. A clear spectral hardening, namely an increase in the flux spectral index, is observed for both primary and secondary species above 200 GV [1]. The study of the B/C flux ratio, widely used to study the propagation of galactic cosmic rays, i.e., in the GeV to TeV energy range, has provided solid indications for the diffusion to be responsible for this feature [10, 29, 35, 38].

In this work, we have followed the method presented in [29], and we have used the USINE code to study the effect of cross-sections on the determination of propagation parameters from the B/C data from the AMS-02 experiment. We use a two-break diffusion coefficient as described in the literature. We generated and analysed mock data comparable to the B/C measurements, and we compared the mock data to three benchmark models, BIG, SLIM, and QUAINT available in the literature. We find that we can retrieve the true values of the transport parameters for a conventional scenario in which we only use statistical uncertainties. Moreover, we find that assuming the wrong cross-sections can bias the transport parameters significantly in the conventional scenario. Adding systematic uncertainties, especially relevant in the low rigidity range of the AMS-02 measurements, would reduce cross-section uncertainties on the transport parameters.

Moreover, we studied the propagation parameters using two additional observables: the deuteron flux and the ^{2}H/^{4}He flux ratio. These measurements are helpful to probe the universality of CR propagation in the galaxy. We used the USINE code to generate the model of deuteron flux and studied how the deuteron flux depends on the galactic disk size, the solar modulation effective potential, the choice of the transport model, and various physical processes relevant to CR propagation through the galaxy. We have found that the deuteron flux is sensitive to the galactic halo size and the strength of the solar modulation effective potential. We have also illustrated how different physical phenomena, such as reacceleration and convection, affect the deuteron flux. Finally, we fitted the deuteron flux and the ^{2}H/^{4}He flux ratio to the current most precise data from the PAMELA experiment to obtain constraints to the propagation parameters. Our results are overall consistent with those obtained in the literature from the B/C flux ratio, even though our best fit results are often less constraining due to the more considerable uncertainties. Because the PAMELA data are only available in a limited range, between 0.1 and 1 GeV/n, it is thus hard to constraint phenomena relevant at higher energies, such as diffusion. For the SLIM model, our results for the high-rigidity diffusion, namely the parameters δ and K_0, are in tension with the results from the literature, which are derived from the B/C. However, our results have significant uncertainties, possibly due to the sizeable uncertainty of the PAMELA data and their limited energy range. The fit result from the QUAINT model hints at the presence of mild reacceleration ($V_a \approx 50$ km s^{-1}) and the absence of convection, i.e., $V_c \approx 0$ km s^{-1}, consistent with the finding from the literature. The fitting procedures for this study did not include cross-sections as nuisance parameters, and it was performed with data on the energy range 0.1 - 1 GeV/n. The inclusion of cross-section nuisance parameters, which is beyond the scope of this work, together with the use of upcoming AMS-02 measurements that will cover an extended range, up to 10 GeV/n, is necessary to obtain stricter constraints on the transport parameters.

A Additional plots of CR fluxes and flux ratios

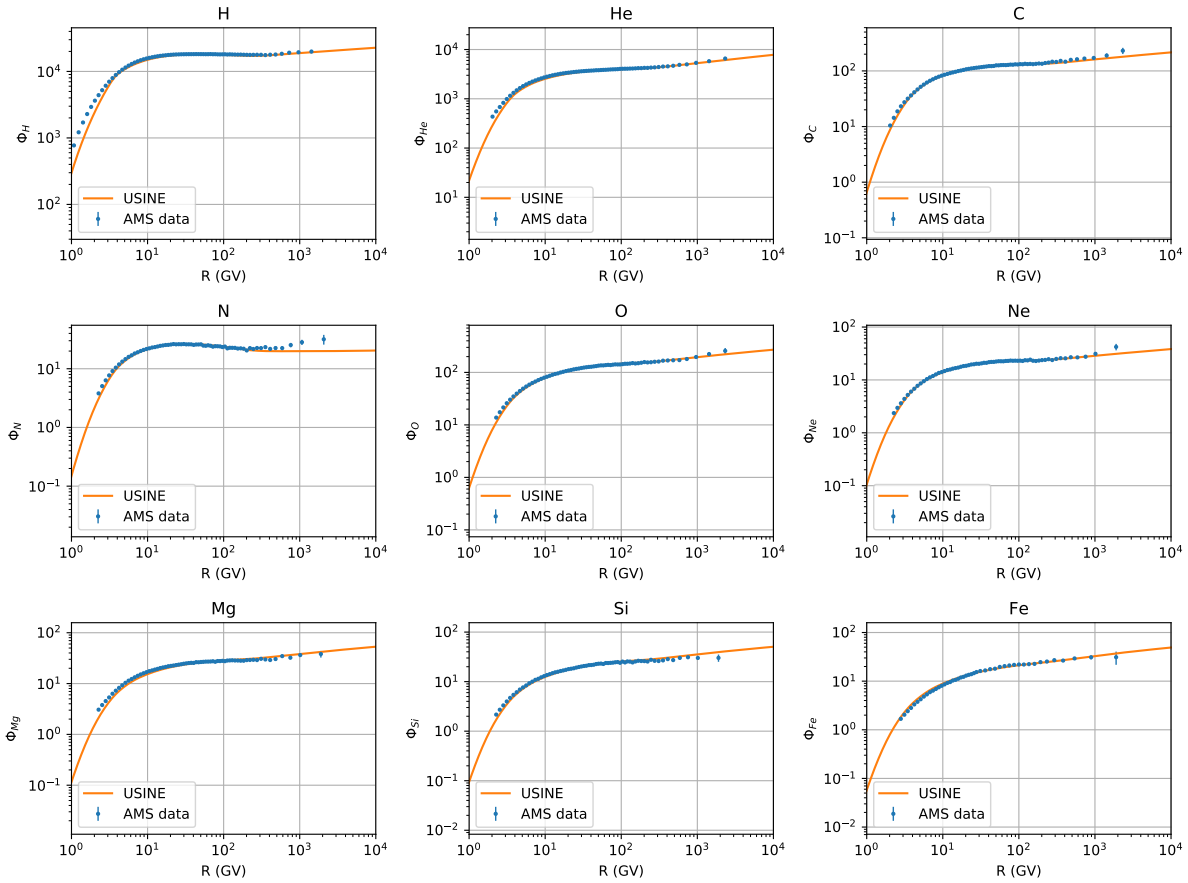

Figure A.1: Fluxes Φ $[\#\,\mathrm{sr}^{-1}\,\mathrm{s}^{-1}\,\mathrm{m}^{-2}\,R^{-1}]$ of various CR species generated by USINE together with the AMS-02 measurements. For AMS-02 data we display the total uncertainty, given by the statistical and systematic uncertainty summed in quadrature.

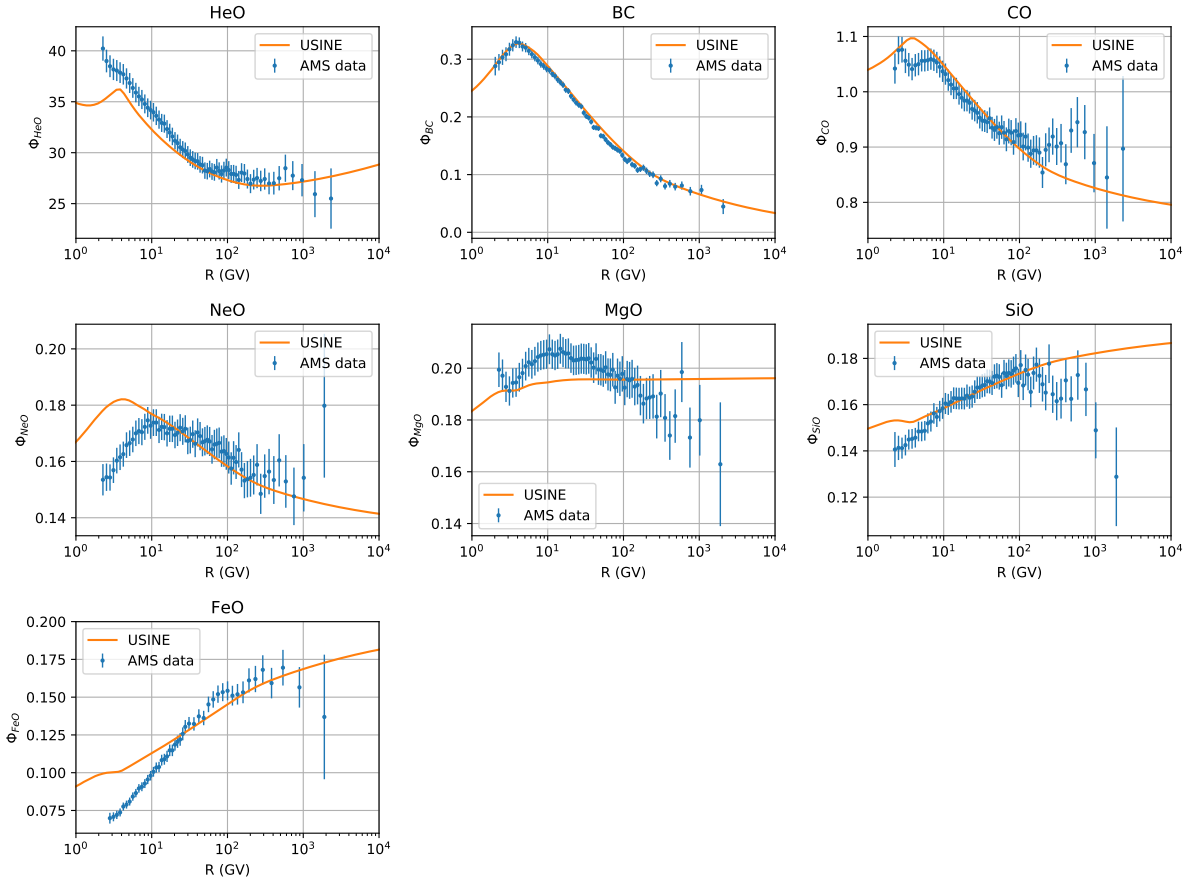

Figure A.2: Flux ratios Φ generated by USINE together with the AMS-02 measurements. For AMS-02 data we display the total uncertainty, given by the statistical and systematic uncertainty summed in quadrature.

References

[1] M Aguilar et al. "The Alpha Magnetic Spectrometer (AMS) on the international space station: Part II—Results from the first seven years". In: *Physics reports* 894 (2021), pages 1–116.

[2] VS Berezinski et al. *Astrophysics of cosmic rays*. Edited by VL Ginzburg. published by North-Holland (Amsterdam), 1990.

[3] WD Apel et al. "Kneelike structure in the spectrum of the heavy component of cosmic rays observed with KASCADE-Grande". In: *Physical Review Letters* 107.17 (2011), page 171104.

[4] K Greisen. "End to the cosmic-ray spectrum?" In: *Physical Review Letters* 16.17 (1966), page 748.

[5] GT Zatsepin and VA Kuz'min. "Upper limit of the spectrum of cosmic rays". In: *Soviet Journal of Experimental and Theoretical Physics Letters* 4 (1966), page 78.

[6] CPDG Patrignani et al. "Review of particle physics". In: *Chinese Physics C* 40.10 (2016), page 100001.

[7] S Mollerach and E Roulet. "Progress in high-energy cosmic ray physics". In: *Progress in Particle and Nuclear Physics* 98 (2018), pages 85–118.

[8] M Aguilar et al. "Precision measurement of the boron to carbon flux ratio in cosmic rays from 1.9 GV to 2.6 TV with the alpha magnetic spectrometer on the international space station". In: *Physical Review Letters* 117.23 (2016), page 231102.

[9] M Aguilar et al. "Observation of new properties of secondary cosmic rays lithium, beryllium, and boron by the alpha magnetic spectrometer on the international space station". In: *Physical review letters* 120.2 (2018), page 021101.

[10] Y Génolini et al. "Indications for a high-rigidity break in the cosmic-ray diffusion coefficient". In: *Physical Review Letters* 119.24 (2017), page 241101.

[11] C Grupen et al. *Astroparticle physics*. Volume 50. Springer, 2005.

[12] F LeBlanc. *An introduction to stellar astrophysics*. John Wiley & Sons, 2011.

[13] EG Berezhko and HJ Völk. "Spectrum of cosmic rays produced in supernova remnants". In: *The Astrophysical Journal Letters* 661.2 (2007), page L175.

[14] X Li et al. "Model-dependent estimate on the connection between fast radio bursts and ultra high energy cosmic rays". In: *The Astrophysical Journal* 797.1 (2014), page 33.

[15] ML Burns and R Lovelace. "Theory of electron-positron showers in double radio sources". In: *The Astrophysical Journal* 262 (1982), pages 87–99.

[16] MS Longair. *High energy astrophysics*. Cambridge university press, 2010.

[17] A De Angelis and M Pimenta. "Messengers from the High-Energy Universe". In: *Introduction to Particle and Astroparticle Physics*. Springer, 2018, pages 575–681.

[18] A De Angelis. *PARTICLE AND ASTROPARTICLE PHYSICS: Problems and Solutions*. SPRINGER, 2021.

[19] A Fick. "V. On liquid diffusion". In: *The London, Edinburgh, and Dublin Philosophical Magazine and Journal of Science* 10.63 (1855), pages 30–39.

[20] R Schlickeiser. *Cosmic Ray Astrophysics*. Springer, 2002.

[21] A Shalchi. *Nonlinear cosmic ray diffusion theories*. Volume 362. Springer, 2009.

[22] P Reichherzer et al. “Turbulence-level dependence of cosmic ray parallel diffusion”. In: *Monthly Notices of the Royal Astronomical Society* 498.4 (2020), pages 5051–5064.

[23] R Blandford and D Eichler. “Particle acceleration at astrophysical shocks: A theory of cosmic ray origin”. In: *Physics Reports* 154.1 (1987), pages 1–75.

[24] D Maurin et al. “Cosmic rays below z= 30 in a diffusion model: new constraints on propagation parameters”. In: *The Astrophysical Journal* 555.2 (2001), page 585.

[25] M Uhlig et al. “Galactic winds driven by cosmic ray streaming”. In: *Monthly Notices of the Royal Astronomical Society* 423.3 (2012), pages 2374–2396.

[26] S Recchia, P Blasi, and G Morlino. “Cosmic ray-driven winds in the Galactic environment and the cosmic ray spectrum”. In: *Monthly Notices of the Royal Astronomical Society* 470.1 (2017), pages 865–881.

[27] AW Strong and IV Moskalenko. “Propagation of cosmic-ray nucleons in the galaxy”. In: *The Astrophysical Journal* 509.1 (1998), page 212.

[28] A Putze, L Derome, and D Maurin. “A Markov Chain Monte Carlo technique to sample transport and source parameters of Galactic cosmic rays-II. Results for the diffusion model combining B/C and radioactive nuclei”. In: *Astronomy & Astrophysics* 516 (2010), A66.

[29] L Derome et al. “Fitting B/C cosmic-ray data in the AMS-02 era: a cookbook-Model numerical precision, data covariance matrix of errors, cross-section nuisance parameters, and mock data”. In: *Astronomy & Astrophysics* 627 (2019), A158.

[30] MS Potgieter. “Solar modulation of cosmic rays”. In: *Living Reviews in Solar Physics* 10.1 (2013), pages 1–66.

[31] A Ghelfi et al. “Neutron monitors and muon detectors for solar modulation studies: 2. ϕ time series”. In: *Advances in Space Research* 60.4 (2017), pages 833–847.

[32] C Corti et al. “Test of validity of the force-field approximation with AMS-02 and PAMELA monthly fluxes”. In: *arXiv preprint arXiv:1910.00027* (2019).

[33] D Maurin. “usine: Semi-analytical models for Galactic cosmic-ray propagation”. In: *Computer Physics Communications* 247 (Feb. 2020), page 106942. ISSN: 0010-4655.

[34] V Bindi et al. “Calibration and performance of the AMS-02 time of flight detector in space”. In: *Nuclear Instruments and Methods in Physics Research Section A: Accelerators, Spectrometers, Detectors and Associated Equipment* 743 (2014), pages 22–29.

[35] Y Genolini et al. “Cosmic-ray transport from AMS-02 boron to carbon ratio data: Benchmark models and interpretation”. In: *Physical Review D* 99.12 (2019), page 123028.

[36] N Weinrich et al. “Galactic halo size in the light of recent AMS-02 data”. In: *Astronomy & Astrophysics* 639 (2020), A74.

[37] F Donato et al. “Antiprotons in cosmic rays from neutralino annihilation”. In: *Phys. Rev. D* 69 (6 Mar. 2004), page 063501.

[38] N Weinrich et al. “Combined analysis of AMS-02 (Li, Be, B)/C, N/O, 3He, and 4He data”. In: *Astronomy & Astrophysics* 639 (2020), A131.

[39] Y Génolini et al. “Current status and desired precision of the isotopic production cross sections relevant to astrophysics of cosmic rays: Li, Be, B, C, and N”. In: *Physical Review C* 98.3 (2018), page 034611.

[40] F James and M Roos. "Minuit-a system for function minimization and analysis of the parameter errors and correlations". In: *Computer Physics Communications* 10.6 (1975), pages 343–367.

[41] RK Tripathi, FA Cucinotta, and JW Wilson. "Accurate universal parameterization of absorption cross sections". In: *Nuclear Instruments and Methods in Physics Research Section B: Beam Interactions with Materials and Atoms* 117.4 (1996), pages 347–349.

[42] RK Tripathi, FA Cucinotta, and JW Wilson. "Accurate universal parameterization of absorption cross sections III–light systems". In: *Nuclear Instruments and Methods in Physics Research Section B: Beam Interactions with Materials and Atoms* 155.4 (1999), pages 349–356.

[43] WR Webber et al. "Updated Formula for Calculating Partial Cross Sections for Nuclear Reactions of Nuclei with Z$\leq$ 28 and E$>$ 150 MeV Nucleon–1 in Hydrogen Targets". In: *The Astrophysical Journal Supplement Series* 144.1 (2003), page 153.

[44] HP Wellisch and D Axen. "Total reaction cross section calculations in proton-nucleus scattering". In: *Physical Review C* 54.3 (1996), page 1329.

[45] IV Moskalenko, SG Mashnik, and AW Strong. "New calculation of radioactive secondaries in cosmic rays". In: *arXiv preprint astro-ph/0106502* (2001).

[46] IV Moskalenko and SG Mashnik. "Evaluation of production cross sections of Li, Be, B in CR". In: *arXiv preprint astro-ph/0306367* (2003).

[47] O Adriani et al. "Measurements of cosmic-ray hydrogen and helium isotopes with the PAMELA experiment". In: *The Astrophysical Journal* 818.1 (2016), page 68.

[48] N Tomassetti and J Feng. "The curious case of high-energy deuterons in Galactic cosmic rays". In: *The Astrophysical Journal Letters* 835.2 (2017), page L26.

[49] B Coste et al. "Constraining Galactic cosmic-ray parameters with Z$\leq$2 nuclei". In: *Astronomy & Astrophysics* 539 (Feb. 2012), A88. ISSN: 1432-0746.

[50] D Maurin, F Melot, and R Taillet. "A database of charged cosmic rays". In: *Astronomy & Astrophysics* 569 (2014), A32.

[51] M Aguilar et al. "The Alpha Magnetic Spectrometer (AMS) on the International Space Station: Part I–results from the test flight on the space shuttle". In: *Physics Reports* 366.6 (2002), pages 331–405.